

Summer 8-22-2021

LONG TERM VARIATION OF CLASS I METHANOL MASERS

Nycole Wenner

DePaul University, nwenner@depaul.edu

Follow this and additional works at: https://via.library.depaul.edu/csh_etd

 Part of the [Physics Commons](#)

Recommended Citation

Wenner, Nycole, "LONG TERM VARIATION OF CLASS I METHANOL MASERS" (2021). *College of Science and Health Theses and Dissertations*. 386.

https://via.library.depaul.edu/csh_etd/386

This Thesis is brought to you for free and open access by the College of Science and Health at Via Sapientiae. It has been accepted for inclusion in College of Science and Health Theses and Dissertations by an authorized administrator of Via Sapientiae. For more information, please contact digitalservices@depaul.edu.

LONG TERM VARIATION OF CLASS I METHANOL MASERS

A Thesis
Presented in
Partial Fulfillment of the
Requirements for the Degree of
MASTER OF SCIENCE

July, 2 0 2 1

BY
Nycole Wenner

PHYSICS DEPARTMENT
College of Science and Health
DePaul University
Chicago, Illinois

ACKNOWLEDGEMENTS

I would like to acknowledge my thesis advisor Dr. Anuj Sarma for allowing me to join his project and use the data he took for my own thesis project. I would also like to acknowledge my thesis committee members Dr. Jesus Pando and Dr. Bernhard Beck-Winchatz for their help and support. I thank the DePaul Physics Department for their support throughout this process. I would also like to thank Dr. Emmanuel Momjian of the National Radio Astronomy Observatory for acting as my supervisor over the previous summer, and the National Radio Astronomy Observatory for the Summer Student Research Assistantship grant at the Karl G. Jansky Very Large Array in New Mexico that allowed me to conduct this research. Lastly, I would like to thank my family and friends for the emotional support throughout this process, particularly Colin McGreevy and Dan Kabat.

TABLE OF CONTENTS

LIST OF FIGURES	4
LIST OF TABLES	6
ABSTRACT	7
CHAPTER 1 Introduction	8
1.1 Masers	10
1.1.1 Maser Formation	10
1.1.2 Interstellar Masers	12
1.2 Methanol (CH ₃ OH) masers	12
1.2.1 Class I CH ₃ OH Masers	12
1.3 The High Mass Star Forming Region DR21(OH)	14
CHAPTER 2 Observations and Data Reduction	18
2.1 The 2017 Observations	18
2.2 The 2001 Observations	21
2.3 The 2012 Observations	22
CHAPTER 3 Results	23
3.1 Results from the 2017 Observations	23
3.1.1 Individual Masers	27
3.2 Results from the 2001 Observations	47
3.3 Results from the 2012 Observations	47
CHAPTER 4 Discussion	58
4.1 Maser Distribution	58
4.2 Maser Variability	60
4.2.1 The two strongest masers: Maser 4 and Maser 30	61
4.2.2 Masers in the outer arc of the western lobe	63
4.2.3 Masers in the inner arc of the western lobe	65
4.2.4 Masers in the inner arc of the eastern lobe	66
4.2.5 Masers in the outer arc of the eastern lobe	66
4.3 Reasons for maser variability	67
CHAPTER 5 Conclusions and Future Work	70

LIST OF FIGURES

1.1	Stimulated emission in a maser transition.	10
1.2	Maser amplification along velocity-coherent column of gas.	11
1.3	Image of the Cygnus-X molecular cloud complex taken with Herschel.	15
1.4	Contour image of the DR21 ridge taken with the MAMBO camera on the IRAM telescope at a wavelength of 1.2 mm.	16
3.1	Locations of the 57 Class I CH ₃ OH maser spots at 44 GHz in the high mass star forming region DR21(OH) from the 2017 observations.	24
3.2	Figure showing the masers in the region enclosed by the dashed rect- angle in Figure 3.1.	25
3.3	Map of masers as in Figure 3.2 but with the inner and outer arcs in each lobe marked.	26
3.4	Observed profile at 44 GHz of the Class I CH ₃ OH line toward DR21(OH) designated as maser 4 in Table 3.1, fitted Gaussian com- ponents and their sum, and residuals from the fit.	28
3.5	Observed profile at 44 GHz of the Class I CH ₃ OH line toward DR21(OH) designated as maser 5 in Table 3.1, fitted Gaussian com- ponent, and residuals from the fit.	29
3.6	Observed profile, Gaussian components and residuals as in Figure 3.4, but for maser 6 in Table 3.1.	30
3.7	Observed profile, Gaussian component and residuals as in Figure 3.5, but for maser 11 in Table 3.1.	31
3.8	Observed profile, Gaussian components and residuals as in Figure 3.4, but for maser 15 in Table 3.1.	32
3.9	Observed profile, three fitted Gaussian components and their sum, and the residuals from the fit for maser 18 in Table 3.1.	33
3.10	Observed profile, Gaussian components and residuals as in Figure 3.4, but for maser 19 in Table 3.1.	35
3.11	Observed profile, Gaussian components and residuals as in Figure 3.4, but for maser 20 in Table 3.1.	36
3.12	Observed profile, Gaussian components and residuals as in Figure 3.4, but for maser 25 in Table 3.1.	37
3.13	Observed profile, Gaussian components and residuals as in Figure 3.4, but for maser 30 in Table 3.1.	38
3.14	Observed profile, Gaussian components and residuals as in Figure 3.4, but for maser 33 in Table 3.1.	39

LIST OF FIGURES – Continued

3.15 Observed profile, four fitted Gaussian components and their sum, and the residuals from the fit for maser 36 in Table 3.1.	40
3.16 Observed profile, Gaussian components and residuals as in Figure 3.4, but for maser 43 in Table 3.1.	41
3.17 Observed profile, Gaussian component and residuals as in Figure 3.5, but for maser 48 in Table 3.1.	42
3.18 Observed profile, Gaussian component and residuals as in Figure 3.5, but for maser 49 in Table 3.1.	43
3.19 Observed profile, Gaussian components and residuals as in Figure 3.4, but for maser 51 in Table 3.1.	44
3.20 Observed profile, Gaussian component and residuals as in Figure 3.5, but for maser 53 in Table 3.1.	45
3.21 Observed profile, Gaussian components and residuals as in Figure 3.4, but for maser 56 in Table 3.1.	46
4.1 Figure showing the locations of all the masers across all three epochs (2001, 2012, and 2017).	59

LIST OF TABLES

2.1	Parameters for 2017 VLA Observations	19
3.1	Fitted parameters of the 44 GHz Class I CH ₃ OH Masers in DR21(OH) observed in 2017	48
3.2	Masers in DR21(OH) from 2001 observations	54
3.3	Masers in DR21(OH) from 2012 observations	56
4.1	Masers in inner and outer arcs of western and eastern lobes	63

ABSTRACT

Class I methanol (CH_3OH) masers in high mass star forming regions are generally found in outflows. There, shocks provide the collisional pumping that causes the population inversion necessary for maser action. Less is known about Class I methanol masers compared to Class II. A better understanding of Class I masers will allow them to be used as more effective probes of high mass star formation, about which much remains to be learned. In particular, the variability of these masers could potentially be used to investigate activity in high mass star forming regions. I present an investigation of the long-term variability of Class I methanol masers at 44 GHz toward the high mass star forming region DR21(OH). This study uses data from three epochs. Analysis of data observed in 2017 was compared to data observed in 2012, and data taken from the literature in 2001. All the data were observed with the Karl G. Jansky Very Large Array (VLA). A total of 57 maser spots were found in the 2017 data, with center velocities ranging between -8.65 km s^{-1} to $+2.56 \text{ km s}^{-1}$. The masers are arranged in a western and an eastern lobe, with two arcs in each lobe that look like bowshocks, consistent with previous observations. Based on those masers for which data are available for all three epochs, most masers appear to have increased in intensity from 2001 to 2012, then decreased in intensity from 2012 to 2017. Activity in the inner arc of the western lobe appears to be more intense than in the outer arc. I speculate that this may be a consequence of episodic accretion, in which a later accretion event has resulted in ejection of material whose shock reached the inner arc at some point in time after 2001. This thesis establishes that class I methanol masers are variable on long timescales (of the order of 5-10 years).

CHAPTER 1

Introduction

Masers are bright, compact sources, making them ideal for observing high mass¹ star forming regions at high angular resolution. High mass stars play an important role in shaping their surroundings and the entire galaxy, but understanding the formation of high mass stars remains a challenge. A better understanding of maser properties makes them more effective probes of high mass star forming regions. One such observable property is the variability of masers. This thesis presents a dedicated investigation of the variability of Class I methanol (CH_3OH) masers (at 44 GHz) in the high mass star forming region DR21(OH).

During their formation and throughout their lifetime, high mass stars drive outflows, sending tremendous amounts of mass and momentum into the Interstellar Medium. Certain elements can only be formed in high mass stars or in supernovae. High mass stars also accrete high amounts of mass in their nebula, limiting the size of other stars forming in their region. In ways such as these, they modify their surroundings and impact the evolution of the entire galaxy. However, observing the formation of high mass stars remains a challenge because they are farther away from us and form in clusters. These conditions together require higher angular resolution to understand and interpret the observations. That high mass stars are located farther away from us is something we would expect on statistical grounds because of their rarity. High mass stars are only a small fraction of the stellar population. Indeed, the nearest low mass star forming region in Taurus is 140 pc away, but the nearest high mass star forming region in Orion is 450 pc away. High mass stars also form in clusters, and never in isolation, and whether this occurrence in clusters has something to do

¹Stars with masses of $8 M_{\odot}$, or greater, are known as high mass stars.

with how they form remains an unresolved question. Also, since high mass stars go through their evolutionary stages faster than low mass stars, another impact of their rarity is that there are very few examples of a forming high mass star in any given stage of its evolution, so it is difficult to find enough examples to establish an evolutionary sequence.

Several molecules produce maser emission in star forming regions (Section 1.1.2). In particular, Class I CH₃OH masers may be unique tracers of the very early stages of high mass star formation. Maser observations allow for a better understanding of the formation and development of masers, which in turn makes them more useful probes of high mass star forming regions. One example of the maser phenomenon that is observable is the variability of masers. Indeed, the connection of the variability of so-called Class II CH₃OH masers to changes in the radiative output of high mass protostars has already been probed (e.g., Hunter et al. 2018). Although the variability of the other kind of CH₃OH maser, Class I CH₃OH masers, has been hinted at in the literature (Section 1.2.1), there appear to be no papers focused directly on this aspect. The aim of this thesis is to establish that Class I CH₃OH masers in a high mass star forming region are indeed variable. This will be done by analyzing data observed in 2017, comparing it to data observed in 2012, and to published data in the literature observed in 2001.

The rest of this chapter introduces the necessary background information on masers, their formation, and various types of interstellar masers (Sec. 1.1). Methanol masers are then discussed in Section 1.2, and the high mass star forming region DR21(OH) in which Class I methanol masers were observed for this thesis is described in Section 1.3. Details of the observations, reduction, and analysis of the 2017 data are presented in Chapter 2; also included in this chapter is a brief discussion of the 2001 and 2012 data taken from the literature. The results are presented in Chapter 3. Chapter 4 presents a discussion of the results, and conclusions are presented in Chapter 5.

1.1 Masers

The word MASER is an acronym for Microwave Amplification of the Stimulated Emission of Radiation. Although the first astronomical maser was discovered in 1963 (Section 1.1.2), the first laboratory maser was created by Charles Townes and his research team at Columbia nine years earlier in 1954 (Gordon et al., 1955). Masers came before the laser (Light Amplification of the Stimulated Emission of Radiation), and the difference between the two is that masers have longer wavelengths than lasers. Masers have wavelengths that are in the microwave end of the spectrum, while lasers are in the visible, ultraviolet, and infrared parts of the spectrum.

1.1.1 Maser Formation

Maser formation involves three steps: population inversion, stimulated emission, and amplification. Masers are formed when populations of molecules are pumped into a state of population inversion, as is seen in Figure 1.1. Population inversion in a maser is when the majority of the molecules populating a maser transition are in the higher excited state rather than the lower one; population inversion is necessary for a maser to exist. There are two different pumping processes that cause population inversion in astronomical masers to occur; collisional pumping and radiative pumping. Collisional pumping is when the molecules are pumped into an excited state by collisions, which can happen when matter in outflows in star forming regions bumps up against ambient interstellar matter. Radiatively pumped masers form when populations of molecules are bombarded by radiation from their host protostar.

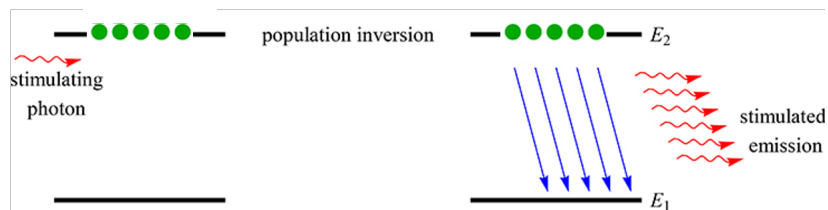


Figure 1.1: Stimulated emission taking place in a maser transition.

As the masers are pumped into a state of population inversion, stimulated emission begins to occur. Stimulated emission is the process by which an incoming photon of a specific frequency can interact with an excited molecule, causing it to drop to a lower energy level. As one stimulating photon comes in, it knocks out another photon, so then there are two identical photons. The two identical photons then interact with more excited molecules and make four identical photons from knocking those molecules into the lower excited state, and the process continues along the pathlength, resulting in maser emission.

In the laboratory, this chain of stimulated emission is set up by repeatedly reflecting the maser or laser signal between mirrors. In star forming regions, the amplification takes place along a long, narrow path in which the required velocity coherence exists (Figure 1.2). Such velocity coherence will exist only along some directions, and that is why maser amplification takes place along some paths and not everywhere. Since masers are amplified along a narrow path, a beaming effect is created, which is how we observe masers to be bright, point-like sources in the sky. The intensity of the radiation coming from a maser grows exponentially so long as the pumping process populating the higher energy levels is greater than the growing losses of the stimulated emission (Reid & Moran, 1981). While this is true, the maser is considered to be unsaturated. A maser is considered to be saturated when the stimulated emission rates in the maser transition surpass the pace at which the population inversion is pumped whether it be from radiative sources or collisional sources (Reid & Moran, 1981).

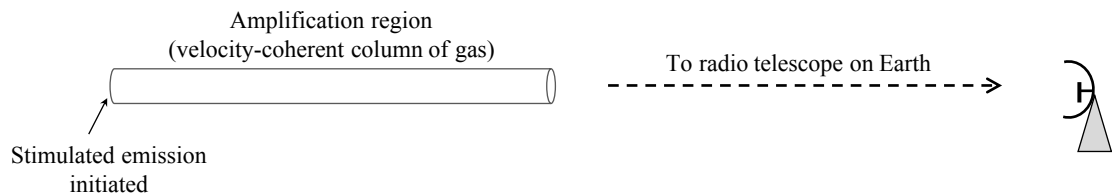


Figure 1.2: Figure showing maser amplification taking place in a velocity-coherent column of gas.

1.1.2 Interstellar Masers

The first interstellar maser detected was an OH maser and was discovered in 1963 (Weaver et al., 1965). Since then, thousands of masers in several different molecules have been discovered in a variety of locations. Such locations include star forming regions, galactic nuclei, and late stage stars, with maser transitions observed in molecules like OH, H₂O, SiO, NH₃, CH₃OH, among others (Elitzur 1992; Gray 2012). This thesis will focus on Class I methanol masers.

1.2 Methanol (CH₃OH) masers

Methanol (CH₃OH) masers come in two types, Class I and Class II (Badrula et al. 1987; Menten 1991). Class II CH₃OH masers are found close to the protostars (e.g., Jones et al. 2020, and references therein) and are radiatively pumped (Sobolev et al. 1997). The most observed Class II CH₃OH maser transition is the 6.7 GHz line (e.g., Green et al. 2017), but there are many other Class II CH₃OH maser lines (see, e.g., Breen et al. 2019, and references therein). Class I CH₃OH masers in star forming regions are usually found in outflows and collisionally pumped (Leurini et al. 2016, and references therein). Most Class I CH₃OH maser observations have been carried out in the 44 GHz line, but observations also exist at 36 GHz, 25 GHz, and 95 GHz (Pratap et al. 2008; Plambeck & Menten 1990).

1.2.1 Class I CH₃OH Masers

Class I CH₃OH masers in star forming regions are usually found in outflows, offset by 0.1 pc to 1 pc from the location of the protostar (McCarthy et al. 2018). Historically, therefore, Class II CH₃OH masers received a lot more attention. As noted by Leurini et al. (2016), that has changed in recent years with the realization that Class I CH₃OH masers are unique tracers of outflows at very early stages in the

high mass star formation process. Thus, there is renewed interest in characterizing the properties of these masers in order to make them more effective probes of high mass star forming regions.

At a minimum, observations of bright Class I CH₃OH masers indicate the presence of a high mass star forming region. Since they form in outflows, Class I CH₃OH masers also provide information on the outflows at a very early stage of the star formation process, including information such as the outflow speed that can be compared to characteristics of the outflow measured by other tracers. Assuming also that Class I CH₃OH maser lines at different frequencies (e.g., 44 GHz and 95 GHz) originate from the same region, we can measure the physical properties of these regions. Particularly in high mass star forming regions, this is important because larger scale thermal emission may not be observable with such high angular resolution.

A relevant characteristic of Class I CH₃OH masers is their variability in intensity, since such variability could potentially be linked to changes in their parent star forming region. Although hints of variability appear in several papers, no dedicated investigation of the variability of Class I CH₃OH masers has ever been made. Kurtz et al. (2004) observed the 44 GHz Class I CH₃OH maser line in 44 high mass star forming regions. Overall, they didn't find variability with the exception of a maser in the star forming region G11.94-0.62, finding that their observed value of 1.45 Jy at 38 km s⁻¹ to be significantly smaller than the 45 Jy at 35 km s⁻¹ reported by Bachiller et al. (1990), concluding that such a change in intensity could not be due to instrumental changes and must be a result of variability. Rodríguez-Garza et al. (2017) detected Class I CH₃OH maser emission at 44 GHz toward 24 high mass star forming regions with the VLA. Three of these sources had been observed previously with a single dish by Litovchenko et al. (2011), but they did not detect any 44 GHz masers. Therefore, Rodríguez-Garza et al. (2017) consider these to be cases of plausible variability.

This thesis will be a dedicated investigation of the variability of Class I CH₃OH masers at 44 GHz in the star forming region DR21(OH). This high mass star forming region is described in the next section. The Class I CH₃OH masers in DR21(OH) are arranged in a western lobe and an eastern lobe (Kogan & Slysh 1998; Kurtz et al. 2004). In each of these two lobes, the masers are arranged in two arcs (Araya et al., 2009); details, including a figure, are in Chapter 3. Observations of Class I CH₃OH masers at 44 GHz toward DR21(OH) were proposed and carried out by A. P. Sarma and E. Momjian in 2017 with the VLA, based on a flip in the two strongest masers from 2001 to 2012. In their 2001 observations, Araya et al. (2009) observed the strongest maser in the field to be located in the outer arc of the western lobe, while the second strongest maser was located in the inner arc of the western lobe. In 2012, Momjian & Sarma (2017) found that the maser in the inner arc had become the strongest maser, whereas the maser in the outer arc had become the second strongest maser. In addition to an investigation of the variation of the two strongest masers, this thesis will also examine whether the other, lower intensity, Class I CH₃OH masers in DR21(OH) have remained largely at the same position as stable structures, and if their intensities have changed from 2001 to 2012 and 2017.

1.3 The High Mass Star Forming Region DR21(OH)

DR21(OH) is a high mass star forming region located in the Cygnus-X molecular cloud complex. Located nearby at a distance of 1.5 kpc (Rygl et al., 2012), Cygnus-X has become one of the most popular active star forming complexes to observe (see, e.g., Comerón et al. 2020, and references therein). Figure 1.3 shows an image of the Cygnus-X molecular cloud complex taken with Herschel (Schneider et al. 2016). This figure shows a region rich in detail, with numerous filamentary strands of molecular gas, bubble-like features created by small ionized hydrogen regions that locally heat the gas, gas heated on a large scale by high mass stars, and colder extended emission from the molecular cloud.

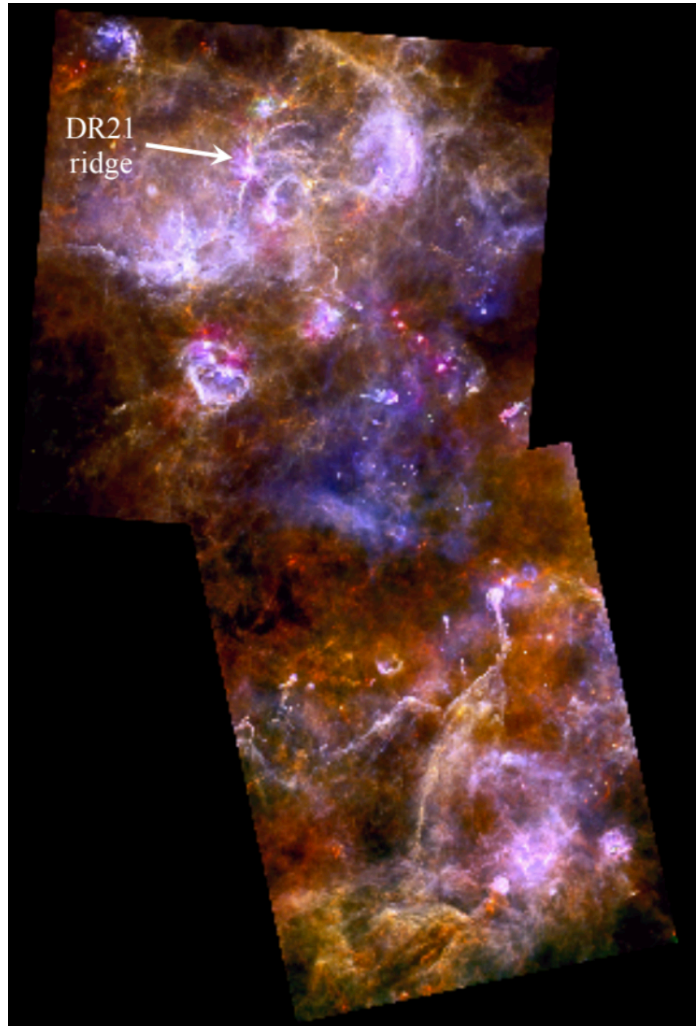


Figure 1.3: Figure adapted from Schneider et al. (2016) showing an image of the Cygnus-X molecular cloud complex taken with Herschel; north is toward the top, and east is to the left. The image covers about 2.8° in RA and 5° in Dec, corresponding to 68 pc and 122 pc respectively. In this three-color image, blue = $70 \mu\text{m}$, green = $160 \mu\text{m}$, and red = $500 \mu\text{m}$. Blue colors indicate gas heated by high mass stars, white colors indicate smaller ionized hydrogen regions that locally heat the gas and create bubble-like features, and red is used to show colder extended emission from the molecular cloud. The 5-pc long filament in the northern part of Cygnus-X, known as the DR21 ridge, is marked.

In the northern part of the image in Figure 1.3, there is a 5-pc long filament known as the DR21 ridge. An enlarged view of the DR21 ridge, taken with the IRAM telescope at a wavelength of 1.2 mm, is shown in Figure 1.4 (Motte et al., 2007). Within the

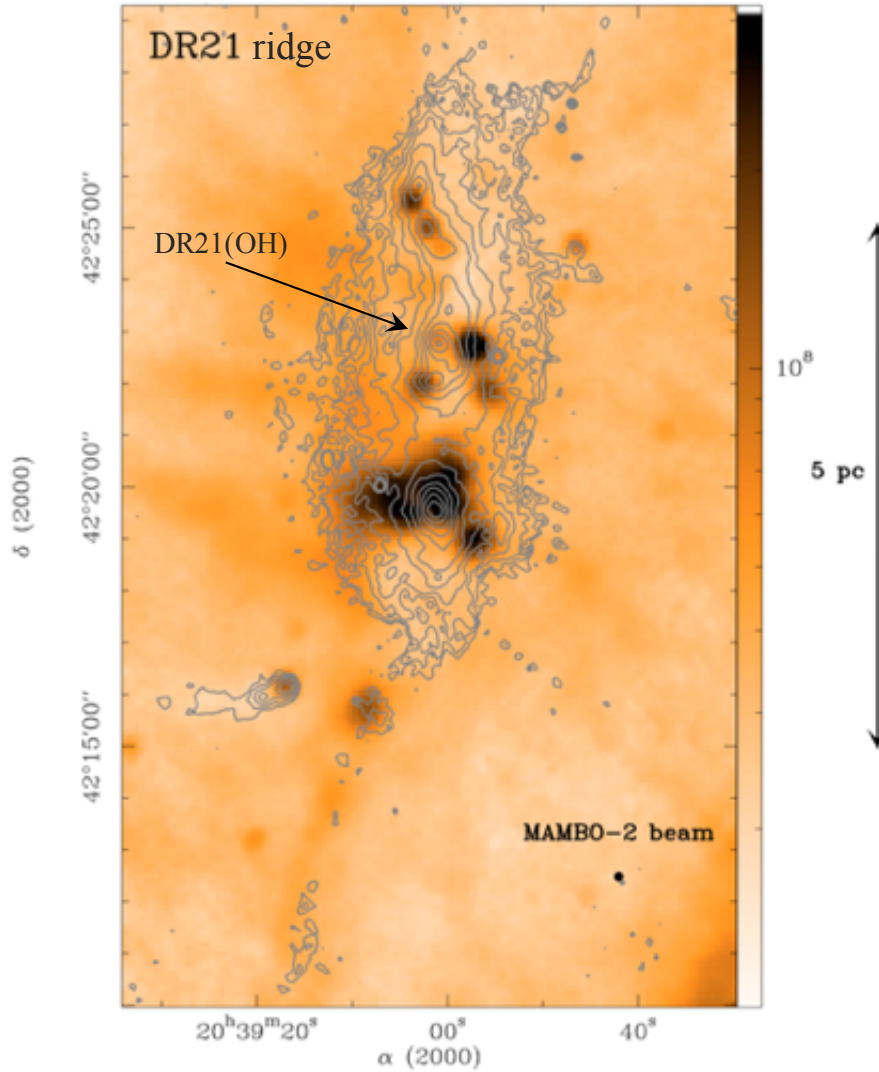


Figure 1.4: Contour image of the DR21 ridge taken with the MAMBO camera on the IRAM telescope at a wavelength of 1.2 mm (Motte et al. 2007), and overlaid on 8 μm images obtained with the Midcourse Space Experiment (MSX). Contour levels are logarithmic and go from 40 to 4800 mJy beam^{-1} . The DR21(OH) source in which Class I CH_3OH masers were observed for this thesis is marked with an arrow.

larger scale 5-pc filament shown in Figure 1.4, the contours pick out several compact cloud fragments; these are massive dense cores in the process of forming high mass stars. One of these is the DR21(OH) source, which is marked in the figure. It has been known for some time that DR21(OH) is in an early stage of high mass star formation. This is because it is not associated with an ionized hydrogen (H II) region, which comes later during the high mass star formation process. Yet, DR21(OH) has several indicators of star formation, including CS thermal emission, bipolar outflows detected in CO emission, and strong Class I CH₃OH masers (Chandler et al. 1993, and references therein). At the center of DR21(OH), high resolution 1.4 mm observations with the Smithsonian Millimeter Array (SMA) reveal about ten compact millimeter sources with masses up to 25 M_{\odot} (Zapata et al., 2012). The arcs traced by the Class I CH₃OH masers (discussed in Section 1.2.1) correspond to bow shocks created by outflows from one of these sources. These bow-shocked structures are also traced by millimeter thermal emission lines of formaldehyde (H₂CO) and CH₃OH (Zapata et al., 2012).

CHAPTER 2

Observations and Data Reduction

The data reported in this thesis are from three different epochs. All three sets of data were observed with the Karl G. Jansky Very Large Array (VLA). The most recent observations taken in 2017 are the data that I worked on for this thesis and are discussed first in Section 2.1; then, the other two epochs for which data were taken from the published literature are discussed briefly in Sections 2.2 and 2.3.

2.1 The 2017 Observations

The Class I CH₃OH maser transition at 44 GHz toward DR21(OH) was observed with the VLA on 24 May 2017 (proposal code: VLA/17A–038; PI: A. P. Sarma). The VLA in New Mexico is an interferometer made up of 27 radio antennas. It is an interferometer because the signals received at each antenna are electronically combined to produce images and spectra of astronomical objects. Every four to five months, the antennas are moved to new locations; there are four such configurations in which the antennas can be arranged. Each of the four configurations allows for a different angular resolution¹. The most compact configuration (D) gives the lowest angular resolution at a given observing frequency, whereas the most extended configuration (A) gives the highest angular resolution. The 2017 observations discussed in this thesis were taken when the VLA was in C configuration, in which the anten-

¹Angular resolution is the capacity to establish that two sources in the sky are separate and distinct. For a radio telescope with diameter D observing at wavelength λ , the angular resolution is of the order λ/D . For an interferometer like the VLA, D is the distance between the antennas located farthest from each other.

nas are arranged so that the maximum baseline is 3.4 km. This, together with other parameters of the observations, can be found in Table 2.1. The term bandwidth in that table refers to the total frequency coverage of the observations, which was 4 MHz. The channel spacing of the observations can then be obtained by dividing the 4 MHz bandwidth by the number of channels (1024), and was 3.90625 kHz. A frequency interval, $\Delta\nu$, can be expressed in terms of velocity using $\Delta\nu/\nu = \Delta v/c$ (for Galactic observations; the expression will need a relativistic correction for extragalactic observations). Using this, we get that the channel spacing corresponds to 0.0266 km s^{-1} at the rest frequency listed in Table 2.1.

Table 2.1: Parameters for VLA Observations

Parameter	Value
Date	2017 May 24
Configuration	C
R.A. of field center (J2000)	20 ^h 39 ^m 00.8 ^s
Dec. of field center (J2000)	42° 22' 47.00''
Total bandwidth (MHz)	4.0
No. of Channels	1024
Channel spacing (km s ⁻¹)	0.0266
Approx. time on source (min)	81
Rest frequency (GHz)	44.069488
FWHM of synthesized beam	0.58'' × 0.55''
	P.A. = -65.88°
Line rms noise (mJy beam ⁻¹) ^a	14

^a The line rms noise was measured from the image cube using maser line-free channels.

Before analysis of data obtained with interferometers like the VLA can be carried out, the data must be edited, calibrated, and imaged. The initial editing and calibration were done by E. Momjian, and the data were then imaged by A. Sarma. The editing, calibration and imaging were done using the Astronomical Imaging Processing System (AIPS) software² provided by the National Radio Astronomy Observatory (NRAO). At this stage, I joined the project and started searching for masers in the 476 frequency (velocity) channels that had been imaged. The AIPS tasks TVSAD and ISPEC were used to search each of these 476 channels for masers. TVSAD is an interactive task that goes through the dataset channel by channel, identifying regions containing intensity values above a user-specified limit. In the first pass, that limit was set to 1 Jy beam^{-1} . This was an arbitrary limit, imposed with the realization that a second pass would be needed to identify lower intensity maser spots. The output of TVSAD was a file containing the channel number and position of the locations containing intensity above the specified 1 Jy beam^{-1} limit; this information was exported into a text file, which was then imported into an Excel file. Since each frequency (velocity) channel was examined for the presence of (maser) sources, the data had to be sifted through to collate all repeat sources that covered more than one channel. The AIPS task ISPEC was used to plot the spectrum at the pixel numbers identified by TVSAD to verify maser sources. TVSAD was then run a second time with the limit set to 70 mJy beam^{-1} to pick out the lower intensity masers, and the steps described above were repeated. The 70 mJy beam^{-1} corresponds to 5 times the rms noise in the line (Table 2.1). At the end of this process which I finished in June 2020, a total of 57 maser spots were identified in the DR21(OH) high mass star forming region.

After compiling the list of maser sources, the AIPS task XGAUS was used to fit gaussians to the spectral profile at each of these 57 locations. XGAUS is an interactive task that allows the user to pick the location in an image at which the user wishes to do a gaussian fit to the spectral line. The user can choose how many

²AIPS is available at aips.nrao.edu, and is supported by Eric W. Greisen, NRAO.

Gaussian components they wish to fit. Once the fit is declared to be good, XGAUS will output the intensity, velocity at line center, and Full Width at Half Maximum (FWHM) linewidth for the spectral profile at each pixel where the fit was done. The fit was judged to be good by visual inspection of the flatness of the residuals generated by XGAUS. It is worth noting here that the objective of this exercise was not to drive up the number of components to achieve a perfect fit to the observed spectral profile. Instead, the goal was to find whether a single component would be a reasonably good representation of the observed profile, or if it would require two or more components. In several cases, the residuals indicate that additional low intensity components with broad linewidths could also be accommodated to provide an even better fit to the line, but no effort was made to add such components. Several examples of these fits are shown in Chapter 3.

2.2 The 2001 Observations

Of the two datasets to which the 2017 observations will be compared in this thesis, one is from 2001 and was reported in Araya et al. (2009). These observations in 2001 were also carried out with the VLA in C configuration, so they have a similar angular resolution ($0.6''$) as the 2017 observations. The positions of masers can therefore be directly compared between these two epochs. Such comparisons allow us to examine whether masers that existed in 2001 are still present in 2017, and if any new masers have appeared. However, the spectral resolution of the 2001 data is much worse (0.7 km s^{-1} compared to 0.0266 km s^{-1} in 2017). Comparison of intensities to check for variability is more difficult as a result of this significant difference in spectral resolution. Still, we can average channels in velocity in the 2017 data to reduce it to the same velocity resolution as the 2001 data and compare intensities. This was done quantitatively to establish the variability of the two strongest masers in DR21(OH), and qualitatively to examine the variability of all the other masers, and is discussed in more detail in Section 4.2.

2.3 The 2012 Observations

The 2017 data will also be compared to observations taken in 2012. These observations too were carried out with the VLA in C configuration, and are reported in Momjian & Sarma (2017). The objective of the 2012 observations was to search for the Zeeman effect in the 44 GHz CH₃OH masers. To achieve a channel spacing of 0.0266 km s⁻¹ to optimize the search for the Zeeman effect, the 2012 observations had to use a narrower frequency range of 1 MHz; improvements to the VLA correlator that allowed a channel spacing of 0.0266 km s⁻¹ with a frequency range of 4 MHz in 2017 were not available in 2012. The similarity in angular resolution and velocity resolution means that the 2017 observations can be compared directly to the 2012 observations; both positions and intensities of the masers between these two epochs can be compared. The disadvantage of the narrower frequency coverage in 2012 is that only a subset of the masers observed in 2017 can be compared to the masers observed in 2012.

CHAPTER 3

Results

Chapter 3 is dedicated to the results of this project, which is to determine the variability over three epochs of Class I CH₃OH masers at 44 GHz. It will begin with a description in Section 3.1 of the results of the 2017 observations that have not been previously published. Results from the observations in 2001 and 2012 will then be presented in brief in Sections 3.2 and 3.3 respectively.

3.1 Results from the 2017 Observations

As a result of the work described in Chapter 2, a total of 57 Class I methanol maser spots at 44 GHz were identified in the data from the 2017 observations of the high mass star forming region DR21(OH). The location, peak intensity, center velocity, and Full Width at Half Maximum (FWHM) velocity linewidth of these masers are shown in Table 3.1, and their distribution is shown in Figure 3.1. Note that while figures have been inserted as close as possible to the location where they are first mentioned, Table 3.1 has been put at the end of the chapter purely for aesthetic reasons; it is a long table that breaks across several pages. There are two masers with intensities higher than 100 Jy beam⁻¹, 9 masers with intensities 10-100 Jy beam⁻¹, 20 masers with intensities 1-10 Jy beam⁻¹, and the remaining 26 have intensities lower than 1 Jy beam⁻¹ (Table 3.1). The center velocities of these masers are found to range between -8.65 to +2.56 km s⁻¹. FWHM linewidths range from 0.193 km s⁻¹ to 1.01 km s⁻¹, with two exceptions; maser 35 has two components, one of which has a linewidth of 1.59 km s⁻¹, and maser 44 has a linewidth of 2.15 km s⁻¹.

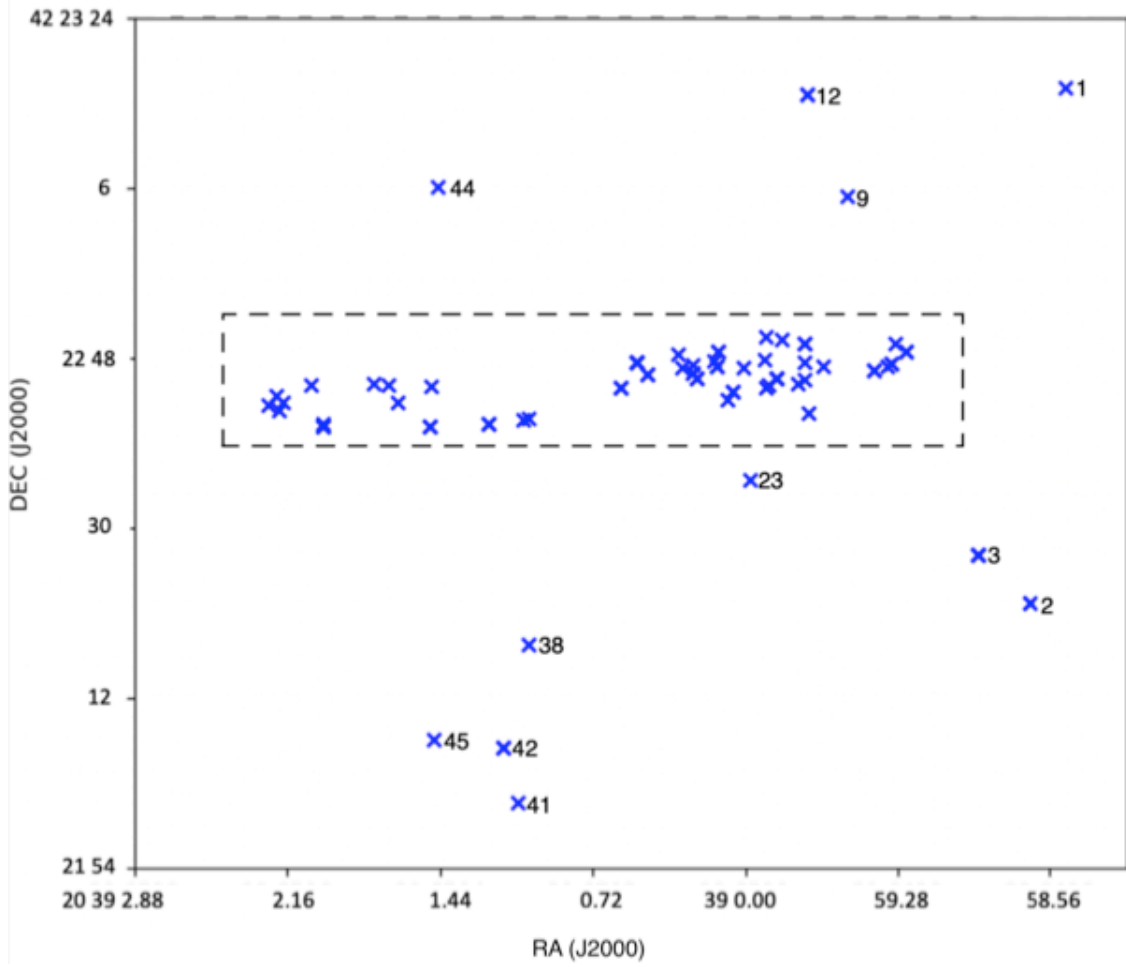


Figure 3.1: Figure showing the locations of the 57 Class I CH₃OH maser spots at 44 GHz in the high mass star forming region DR21(OH) from the 2017 observations. Of these 57 masers, 46 are in the smaller region delineated by the dashed rectangle, and are shown in more detail in Figure 3.2. The remaining 11 masers are to the north and south of the smaller region, and are numbered corresponding to their designation in Table 3.1. The horizontal axis shows the Right Ascension (RA) and the vertical axis shows the Declination (Dec), both in epoch J2000.

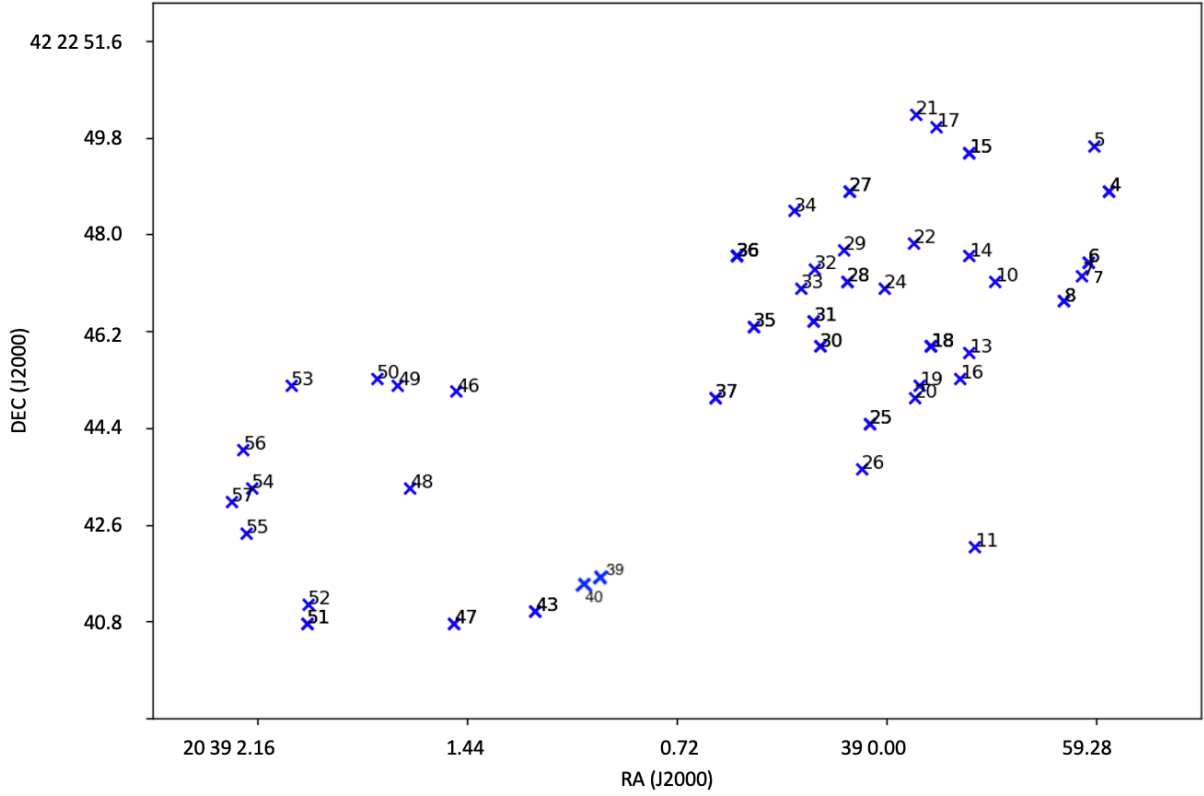


Figure 3.2: Figure showing the masers in the region enclosed by the dashed rectangle in Figure 3.1. The numbers shown beside the position of each maser correspond to their designation in Table 3.1.

Figure 3.1 covers an extent of $51.85''$ in Right Ascension (RA), and $90.0''$ in Declination (Dec), corresponding to 0.38 pc and 0.65 pc respectively¹. We see from this figure that of the 57 maser spots found, 46 are located in a smaller region of size 0.32 pc \times 0.09 pc (enclosed by the dashed rectangle), whereas the remaining 11 masers are located to the north and south of this region. The region enclosed by the dashed rectangle is shown in Figure 3.2, in which the distribution of masers in a western and eastern lobe (Kurtz et al. 2004) becomes apparent. Of the 46 masers in the region enclosed by the dashed rectangle in Figure 3.1, 31 are located in the western lobe in Figure 3.2 (on the right of the image) and 15 in the eastern lobe.

¹At the adopted distance of 1.5 kpc (Rygl et al., 2012) to DR21(OH), $1'' \equiv 0.00727$ pc.

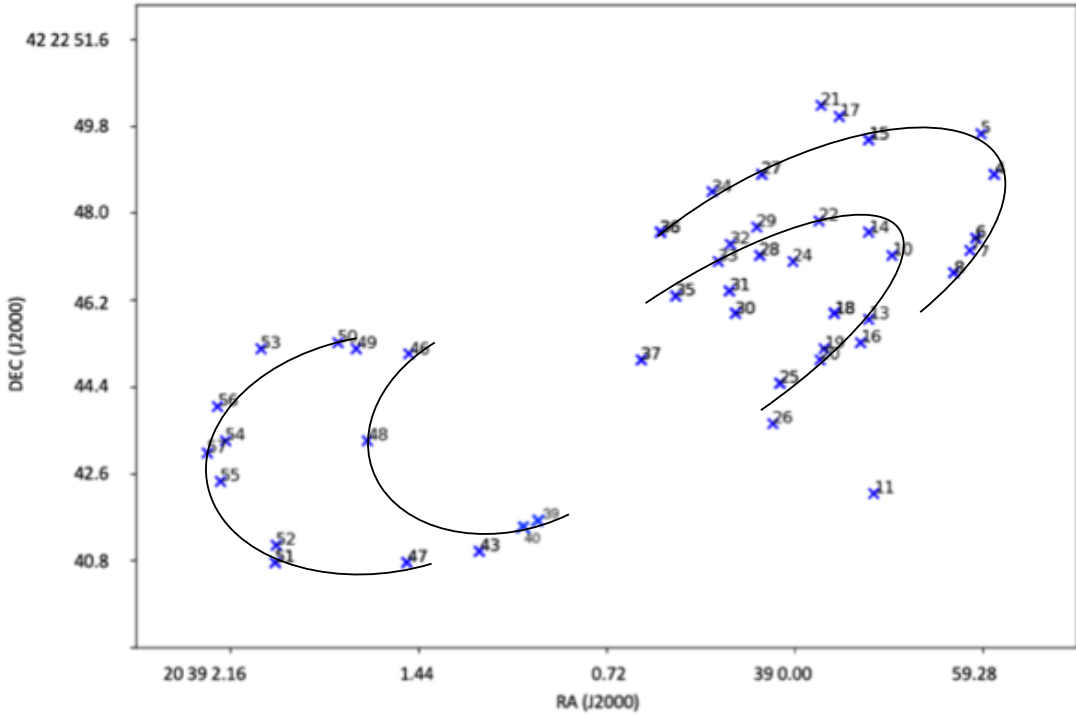


Figure 3.3: Figure showing the masers as in Figure 3.2, but with the inner and outer arcs in each lobe indicated by solid black lines.

Figure 3.2 also reveals that the masers in both the western and eastern lobes are arranged in two arc-like structures in each lobe, in agreement with Araya et al. (2009). These arcs are marked in Figure 3.3 by solid black lines. The outer arc in the western lobe is comprised of 11 masers (masers 36, 34, 27, 21, 17, 15, 5, 4, 6, 7 and 8 in Table 3.1) while the remaining 20 of the 31 masers in the western lobe are in the inner arc (Figure 3.2). The two strongest masers in DR21(OH) are located in the western lobe. Maser 30, the strongest maser, is located in the inner arc of the western lobe and maser 4, the second strongest maser, is located in the outer arc. Both these masers are discussed in more detail in Section 3.1.1. Like the western lobe, masers in the eastern lobe are also present in two arc-like structures although there are fewer masers in this lobe. In the inner arc of the eastern lobe, there are only 5 masers (46, 48, 43, 40, and 39 in Table 3.1), whereas there are 10 masers in the outer arc (Figure 3.2).

In agreement with Kurtz et al. (2004) and Araya et al. (2009), the center velocities of most of the masers in the western lobe are redshifted, whereas the center velocities of most of the masers in the eastern lobe are blueshifted. Note that if a hypothetical source had zero velocity, then masers associated with that source but moving away from us along the line of sight would have positive center velocities, designated as redshifts. Meanwhile, masers moving toward us would have negative center velocities, designated as blueshifts. However, the systemic velocity of DR21(OH) is -3 km s^{-1} , so there is an offset of -3 km s^{-1} in setting the boundary between redshifted and blueshifted velocities. If we think of a number line, then velocities to the right of -3 km s^{-1} are redshifted (that is, all positive velocities and negative velocities up to -3 km s^{-1}), and velocities to the left of -3 km s^{-1} on the number line are blueshifted. The masers in the western lobe are redshifted, with center velocities ranging from 2.561 km s^{-1} to -2.509 km s^{-1} , with the exception of two masers; masers 25 and 26 are blueshifted. In the eastern lobe, the masers are mostly blueshifted, with center velocities ranging from -3.186 km s^{-1} to -6.183 km s^{-1} , with the exception of masers 39, 40, 43, and 46, which are redshifted.

3.1.1 Individual Masers

Individual masers in DR21(OH) are discussed in greater detail in this section. These masers were chosen for further discussion either because they are bright or variable (or both), or have other interesting features. The masers are presented below in the order listed in Table 3.1.

Maser 4

Maser 4 is the second strongest maser in the 2017 observations (Table 3.1), and also in the 2012 observations reported in Momjian & Sarma (2017). Figure 3.4 shows the intensity profile (black histogram-like line) observed in 2017 for this maser. Maser 4 is located in the outer arc of the western lobe as seen in Figure 3.2. The solid green

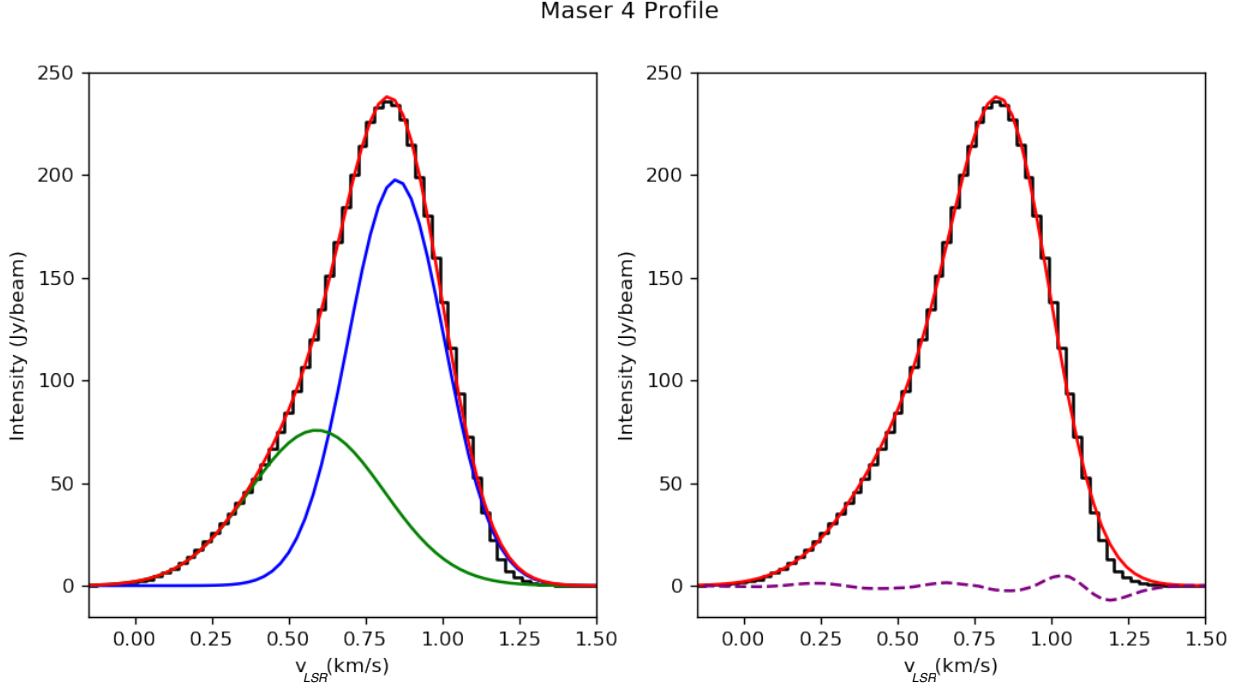


Figure 3.4: Observed profile (black histogram–like line) at 44 GHz of the Class I CH_3OH line toward DR21(OH) designated as maser 4 in Table 3.1. The blue and green curves in the left panel illustrate the Gaussian components fitted to this observed profile. The red curve (in both panels) is the sum of the two Gaussian components shown in the left panel. The dashed purple curve in the right panel is the residual from the fit.

and blue lines in the left panel of Figure 3.4 show the two Gaussian components fitted to this maser profile. The fitted values for both components are listed in Table 3.1. The solid red curve in both panels of Figure 3.4 is the sum of the green and blue Gaussian components, whereas the dashed magenta line in the right panel shows the residuals from the fit. The fits reveal two masers blended in velocity; the stronger (198 Jy beam^{-1}) and narrower (FWHM velocity linewidth 0.368 km s^{-1}) maser is centered at 0.850 km s^{-1} , whereas the lower intensity (76 Jy beam^{-1}) and slightly broader (FWHM velocity linewidth 0.518 km s^{-1}) maser is centered at 0.591 km s^{-1} . The variability of maser 4 is discussed in Section 4.2.1.

Maser 5

Maser 5 is located in the outer arc of the western lobe about $1''$ north of maser 4, and is one of the most red-shifted masers observed in DR21(OH). Figure 3.5 shows the observed profile for this maser. The solid red line in the figure shows the Gaussian component fitted to this maser, whereas the dashed magenta line shows the residual from the fit. The fit reveals a single ($13.65 \text{ Jy beam}^{-1}$) narrow (FWHM velocity linewidth 0.312 km s^{-1}) maser centered at 1.140 km s^{-1} . The variability of maser 5 is discussed in Section 4.2.2.

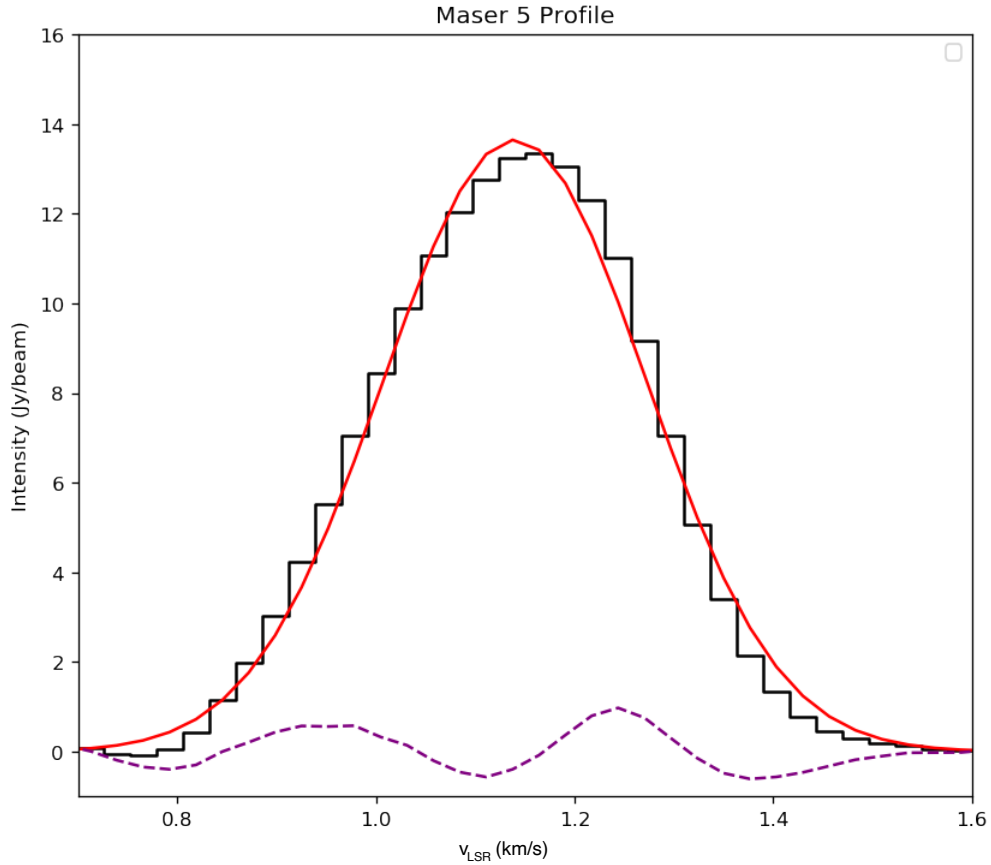


Figure 3.5: Observed profile (black histogram-like line) at 44 GHz of the Class I CH_3OH line toward DR21(OH) designated as maser 5 in Table 3.1. The profile was fitted by a single Gaussian component shown by the red curve; the dashed purple curve shows the residuals from the fit.

Maser 6 Profile

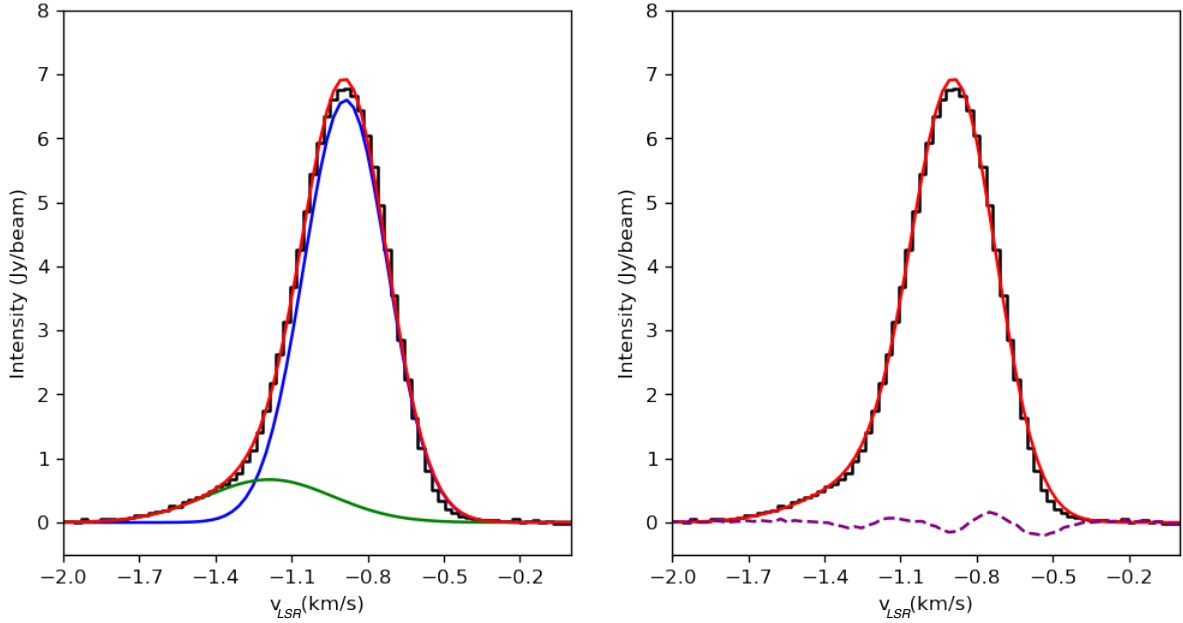


Figure 3.6: Observed profile (black histogram-like line) at 44 GHz toward DR21(OH), fitted Gaussian components (blue and green curves), sum of the fitted Gaussian components (red curve), and residual to the fit (dashed purple curve) as described in Figure 3.4, but for maser 6 listed in Table 3.1.

Maser 6

Maser 6 is located in the outer arc of the western lobe about $1.5''$ south of maser 4; the observed profile for this maser is shown in Figure 3.6. The Gaussian fits listed in Table 3.1 reveal two masers blended in velocity; the stronger ($6.60 \text{ Jy beam}^{-1}$) and narrower (FWHM velocity linewidth 0.389 km s^{-1}) maser is centered at -0.887 km s^{-1} , whereas the lower intensity ($0.67 \text{ Jy beam}^{-1}$) and broader (FWHM velocity linewidth 0.592 km s^{-1}) maser is centered at -1.188 km s^{-1} . The variability of maser 6 is discussed in Section 4.2.2.

Maser 11

Maser 11 is the southernmost maser in the western lobe. Figure 3.7 shows the observed profile for this maser. It was fitted with a single Gaussian component centered at -0.112 km s^{-1} (Table 3.1) which is low in intensity ($0.27 \text{ Jy beam}^{-1}$) but quite narrow (FWHM velocity linewidth 0.486 km s^{-1}). The variability of this maser is discussed in Section 4.2.3.

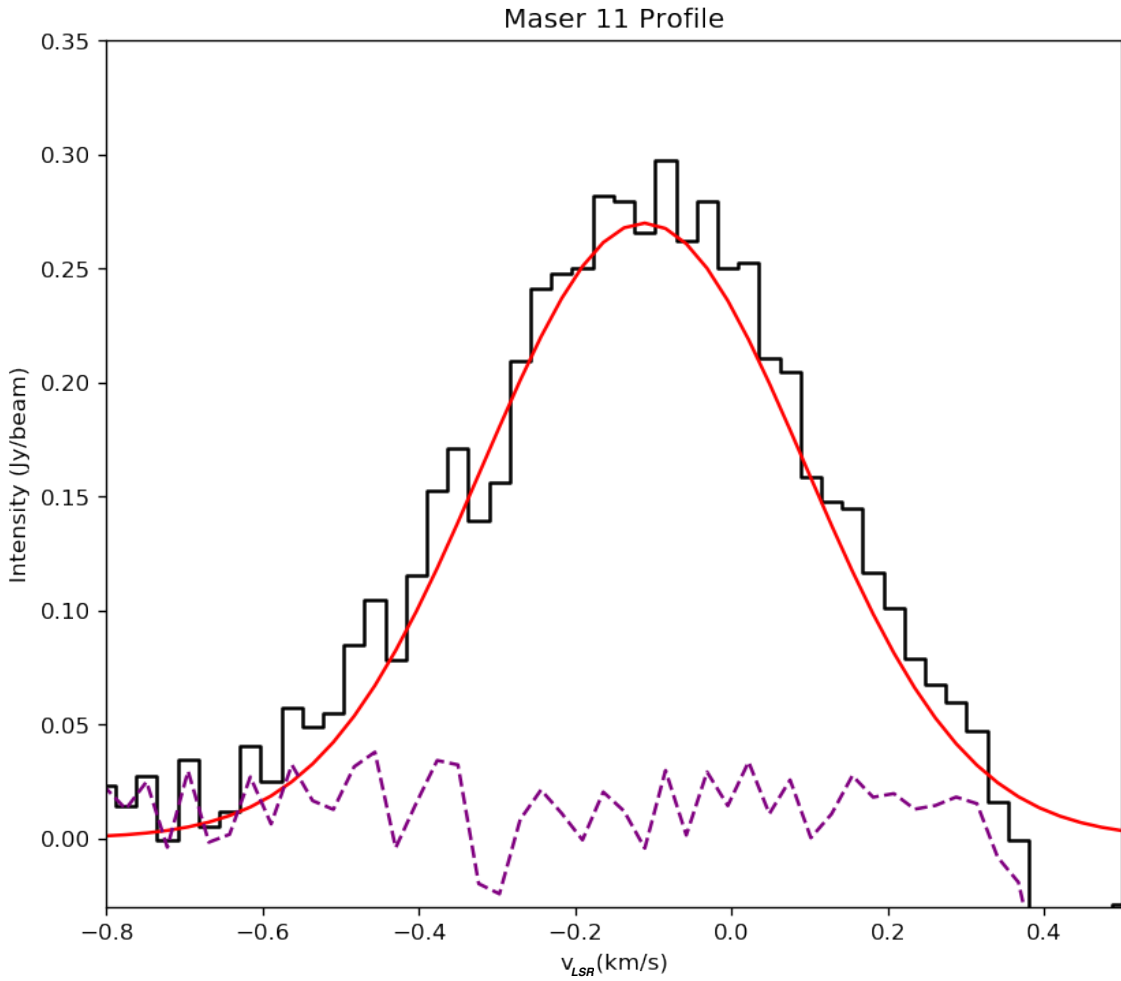


Figure 3.7: Observed profile (black histogram–like line) at 44 GHz of the Class I CH_3OH line toward DR21(OH) designated as maser 11 in Table 3.1. The profile was fitted by a single Gaussian component shown by the red curve; the dashed purple curve shows the residuals from the fit.

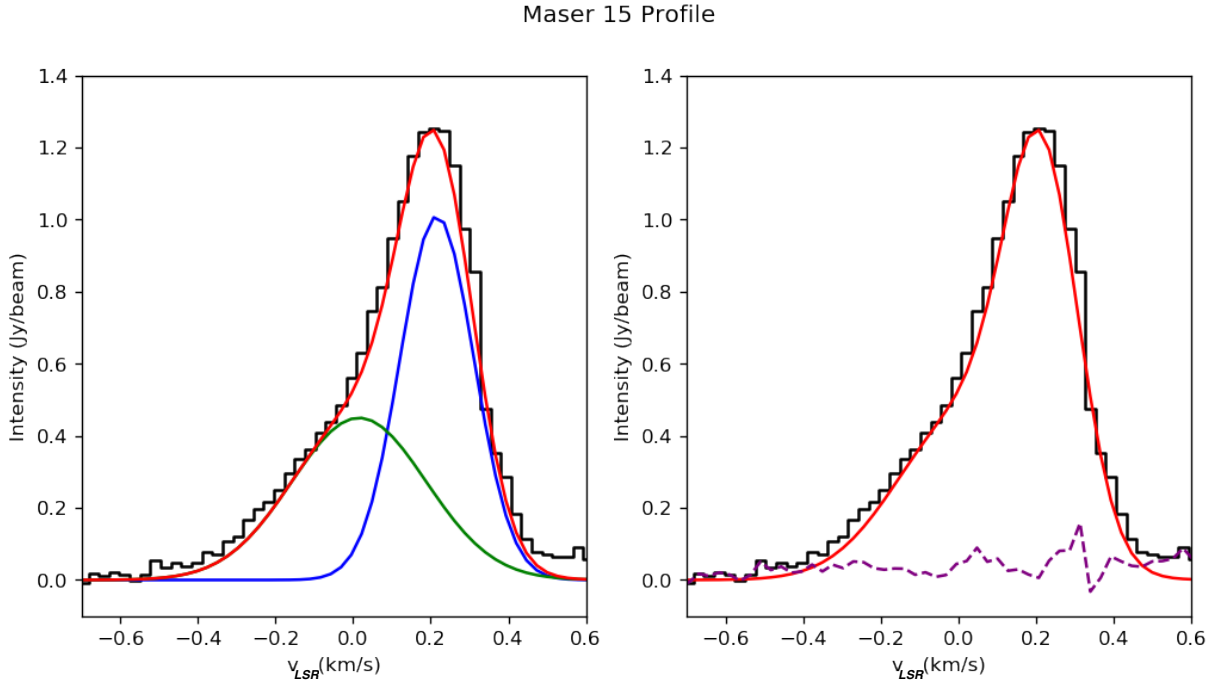


Figure 3.8: Observed profile (black histogram-like line) at 44 GHz toward DR21(OH), fitted Gaussian components (blue and green curves), sum of the fitted Gaussian components (red curve), and residuals from the fit (dashed purple curve) as described in Figure 3.4, but for maser 15 listed in Table 3.1.

Maser 15

Maser 15 is located in the outer arc of the western lobe, and is situated at the base of a finger-like protrusion of two other masers to the northeast (Figure 3.2). The observed profile for maser 15 shown in Figure 3.8 was fitted with two components (Table 3.1). The lower intensity component ($0.45 \text{ Jy beam}^{-1}$) centered at 0.015 km s^{-1} is just under half the intensity of the stronger component ($1.01 \text{ Jy beam}^{-1}$) centered at 0.216 km s^{-1} , but has almost twice the velocity width (FWHM 0.408 km s^{-1} and 0.225 km s^{-1} respectively). Discussion of the variability of maser 15 is given in Section 4.2.2.

Maser 18

Located in the inner arc of the western lobe $4.2''$ west of maser 30, maser 18 was fitted with three Gaussian velocity components (Figure 3.9 and Table 3.1). Of these, the strongest ($12.01 \text{ Jy beam}^{-1}$) and narrowest (FWHM velocity linewidth 0.205 km s^{-1}) component is centered at -0.214 km s^{-1} , whereas the next ($2.78 \text{ Jy beam}^{-1}$) and slightly broader (FWHM velocity linewidth 0.263 km s^{-1}) component is centered at -0.471 km s^{-1} . Finally, the weakest ($2.40 \text{ Jy beam}^{-1}$) and broadest (FWHM velocity linewidth 0.554 km s^{-1}) component is centered at -0.074 km s^{-1} . The variability of these maser components is discussed in Section 4.2.3.

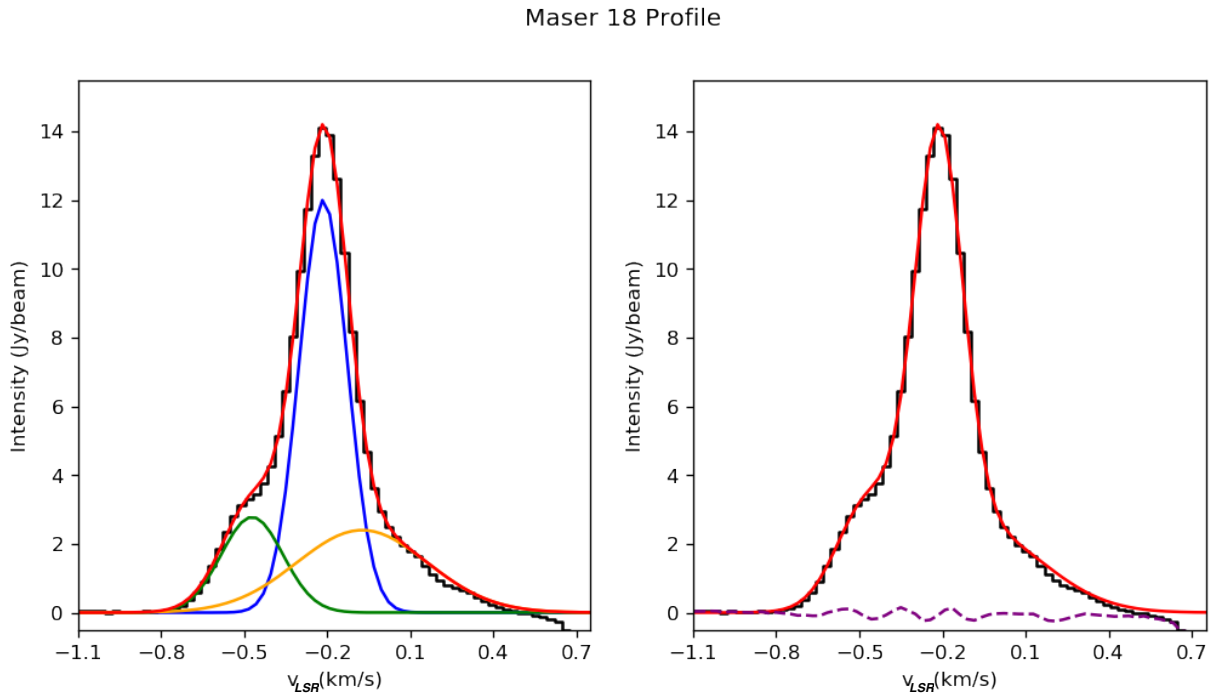


Figure 3.9: Observed profile (black histogram–like line) at 44 GHz of the Class I CH_3OH line toward DR21(OH) designated as maser 18 in Table 3.1. The blue, green and orange curves in the left panel illustrate the Gaussian components fitted to this observed profile. The red curve (in both panels) is the sum of the three Gaussian components shown in the left panel. The dashed purple curve in the right panel is the residual from the fit.

Masers 19 and 20

Masers 19 and 20 display interesting behavior because they are close to each other, separated only by $0.3''$. Both masers are located in the inner arc of the western lobe, with maser 20 largely to the south of maser 19, and slightly to its east (Figure 3.2). At the location of maser 19 (Table 3.1), the observed maser profile is fitted by two Gaussian components (Figure 3.10). Likewise, the observed maser profile at the location of maser 20 is also fitted by two Gaussian components (Figure 3.11). But the component with the lower intensity toward the location of maser 19 has the same center velocity and linewidth as the component with the higher intensity toward the location of maser 20. Therefore, masers 19 and 20 are considered single component masers in this thesis, with the weaker component in each profile belonging to the other maser. Maser 19, with intensity $18.42 \text{ Jy beam}^{-1}$ and FWHM velocity width 0.226 km s^{-1} , is centered at velocity 0.337 km s^{-1} , whereas maser 20, with intensity $16.27 \text{ Jy beam}^{-1}$ and FWHM velocity width 0.203 km s^{-1} , is centered at 0.561 km s^{-1} . The variability of masers 19 and 20 is discussed in Section 4.2.3.

Maser 25

Located in the southern part of the inner arc in the western lobe about $2''$ south of maser 30, maser 25 is the most blue-shifted of all the masers observed. It is interesting for its location, since the western lobe contains mostly redshifted masers. The observed profile for this maser was fitted with two Gaussian components (Figure 3.12). The stronger component with intensity $1.67 \text{ Jy beam}^{-1}$ is narrower (FWHM velocity linewidth 0.326 km s^{-1}) and centered at -8.650 km s^{-1} , whereas the lower intensity component ($0.58 \text{ Jy beam}^{-1}$) is much broader (FWHM velocity linewidth 0.630 km s^{-1}) and is centered at -8.490 km s^{-1} . These highly blueshifted velocities may have something to do with the location of this maser on the very edge of the inner arc of the outflow. Interestingly enough, maser 26 which is located about $0.8''$ to the south of maser 25 is also blueshifted, with a fitted center velocity of -5.112 km s^{-1} .

Maser 19 Profile

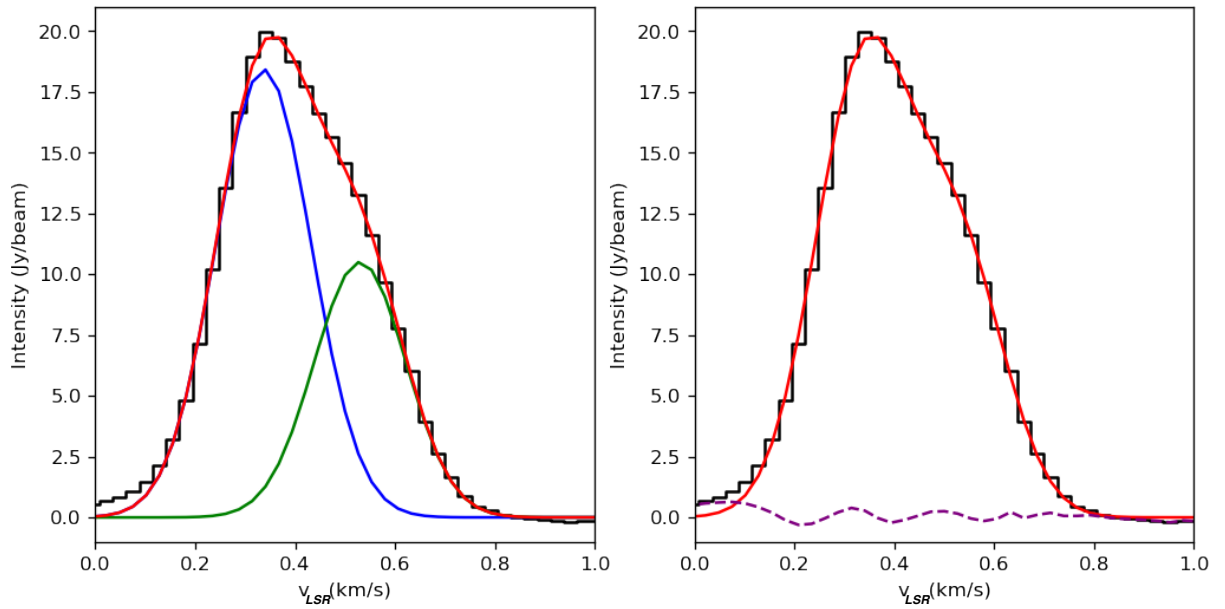


Figure 3.10: Observed profile (black histogram–like line) at 44 GHz of the Class I CH_3OH line toward the position in DR21(OH) designated as maser 19 in Table 3.1. For reasons discussed in Section 3.1.1, the blue curve is designated as the single component profile for maser 19, whereas the green curve corresponds to the nearby maser 20. The red curve (in both panels) is the sum of the blue and green Gaussian components shown in the left panel, whereas the dashed purple curve in the right panel is the residual from the fit.

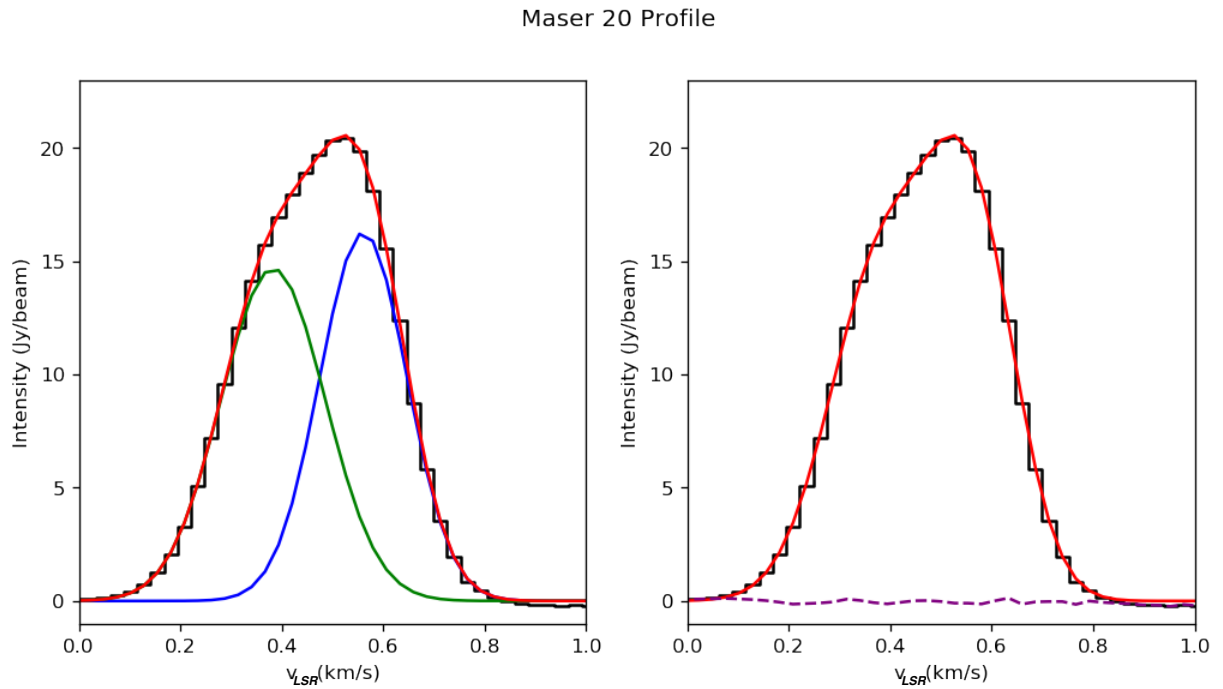


Figure 3.11: Observed profile (black histogram–like line) at 44 GHz of the Class I CH_3OH line toward the position in DR21(OH) designated as maser 20 in Table 3.1. For reasons discussed in Section 3.1.1, the blue curve is designated as the single component profile for maser 20, whereas the green curve corresponds to the nearby maser 19. The red curve (in both panels) is the sum of the blue and green Gaussian components shown in the left panel, whereas the dashed purple curve in the right panel is the residual from the fit.

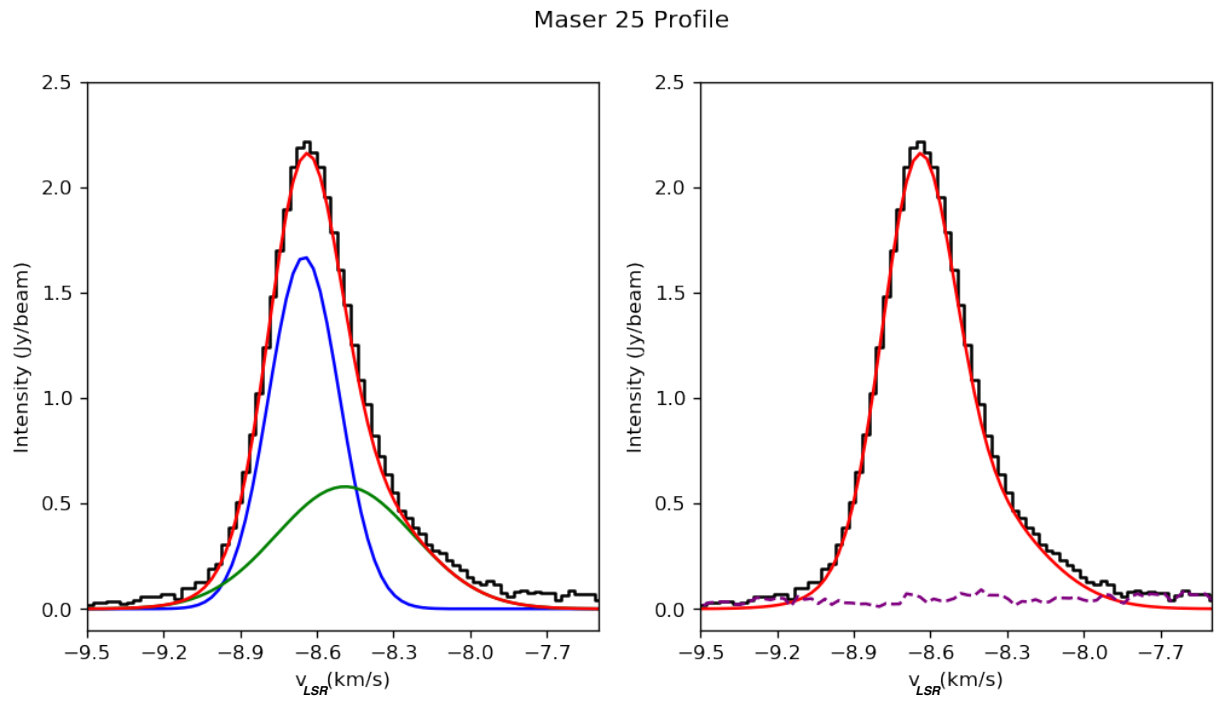


Figure 3.12: Observed profile (black histogram–like line) at 44 GHz toward DR21(OH), fitted Gaussian components (blue and green curves), sum of the fitted Gaussian components (red curve), and residuals from the fit (dashed purple curve) as described in Figure 3.4, but for maser 25 listed in Table 3.1.

Maser 30

Maser 30 is the strongest maser in the field, and is located in the inner arc of the western lobe (Figure 3.2). It was fitted with two Gaussian components (Table 3.1), as shown in Figure 3.13. The stronger and narrower (FWHM velocity linewidth 0.279 km s^{-1}) component has an intensity of 278 Jy beam^{-1} and is centered at 0.465 km s^{-1} , whereas the lower intensity (57 Jy beam^{-1}) and slightly broader (FWHM velocity linewidth 0.316 km s^{-1}) component is centered at 0.205 km s^{-1} . The variability of maser 30 is discussed in Section 4.2.1.

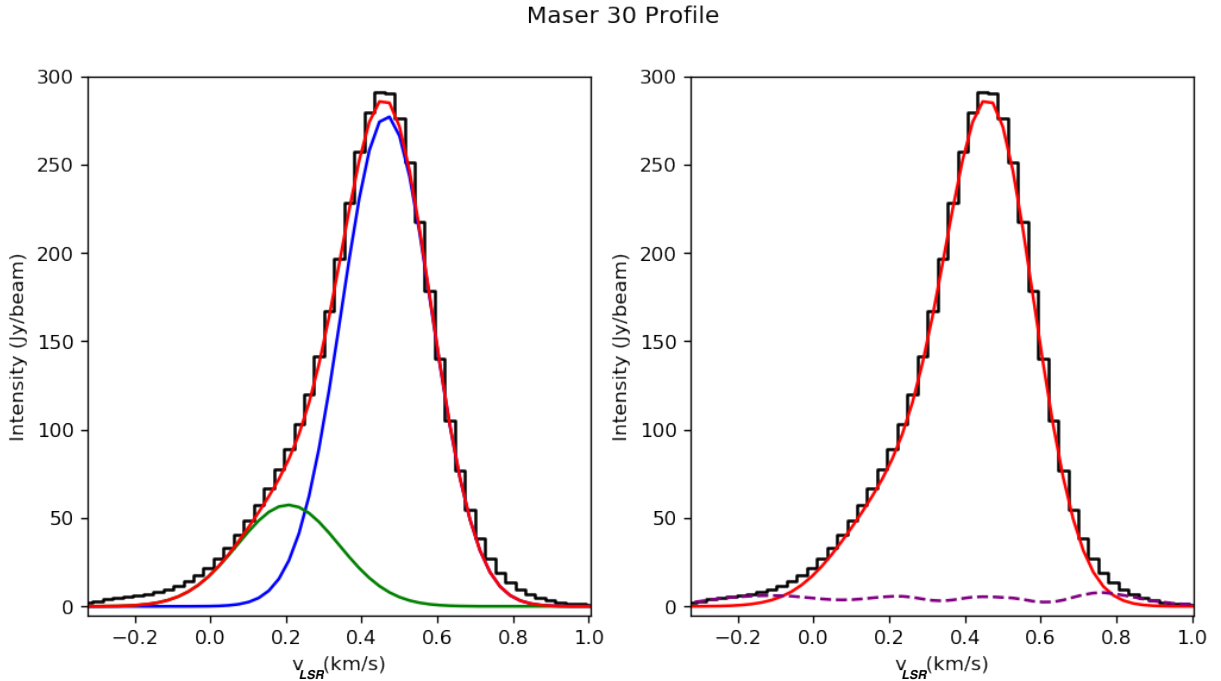


Figure 3.13: Observed profile (black histogram–like line) at 44 GHz toward DR21(OH), fitted Gaussian components (blue and green curves), sum of the fitted Gaussian components (red curve), and residuals from the fit (dashed purple curve) as described in Figure 3.4, but for maser 30 listed in Table 3.1.

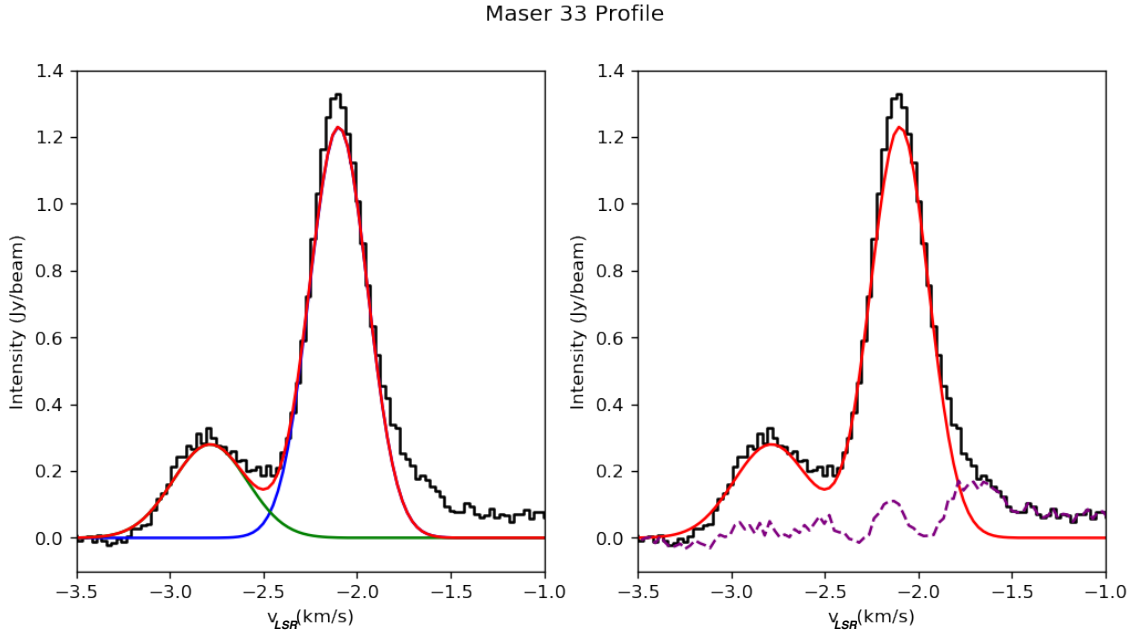


Figure 3.14: Observed profile (black histogram-like line) at 44 GHz of the Class I CH_3OH line toward DR21(OH) at the position designated as maser 33 in Table 3.1. The two velocity components toward this position are almost fully resolved, and have been fitted by Gaussians corresponding to the blue and green curves in the left panel. The red curve (in both panels) is the sum of the blue and green curves shown in the left panel. The dashed purple curve in the right panel is the residual from the fit.

Maser 33

Maser 33 is located on the edge of the inner arc of the western lobe, about $1''$ to the north of maser 30 (Figure 3.2). The observed profile for maser 33 shown in Figure 3.14 was fitted with two components (Table 3.1). The lower intensity component ($0.28 \text{ Jy beam}^{-1}$) centered at -2.786 km s^{-1} has about a quarter of the intensity of the stronger component ($1.23 \text{ Jy beam}^{-1}$) centered at -2.099 km s^{-1} , but is only slightly broader (FWHM 0.417 km s^{-1} and 0.366 km s^{-1} respectively). Discussion of the variability of maser 33 is given in Section 4.2.3.

Maser 36

Located in the outer arc of the western lobe, maser 36 is the most redshifted of all the masers, so much so that on one side it extends beyond the frequency range that was imaged. It required four Gaussian components to be fitted (Figure 3.15), with the strongest component centered at 1.774 km s^{-1} , the second strongest at 2.561 km s^{-1} , the third strongest at 2.137 km s^{-1} , and the weakest at 1.357 km s^{-1} . Intensities and linewidths for these components are given in Table 3.1. The variability of these masers is discussed in Section 4.2.2.

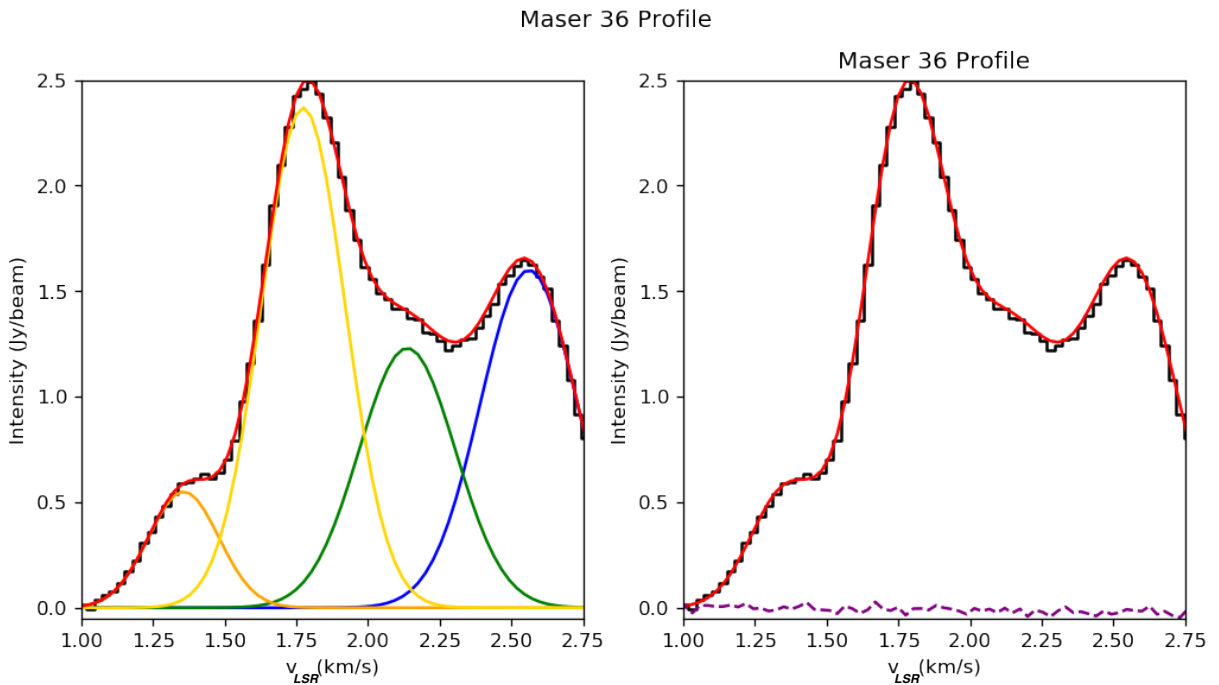


Figure 3.15: Observed profile (black histogram-like line) at 44 GHz of the Class I CH_3OH line toward DR21(OH) designated as maser 36 in Table 3.1. The blue, green, yellow, and orange curves in the left panel illustrate the Gaussian components fitted to this observed profile. The red curve (in both panels) is the sum of the four Gaussian components shown in the left panel. The dashed purple curve in the right panel is the residual from the fit.

Maser 43

Maser 43 is located in the southern part of the inner arc of the eastern lobe (Figure 3.2). The observed profile for this maser was fitted with two Gaussian components (Figure 3.16). The stronger component ($0.56 \text{ Jy beam}^{-1}$) is centered at -2.349 km s^{-1} , and is broader (FWHM velocity linewidth of 0.711 km s^{-1}) than the weaker component ($0.21 \text{ Jy beam}^{-1}$), which is centered at -2.933 km s^{-1} and has a FWHM velocity linewidth of 0.519 km s^{-1} (Table 3.1). The variability of this maser is discussed in Section 4.2.4.

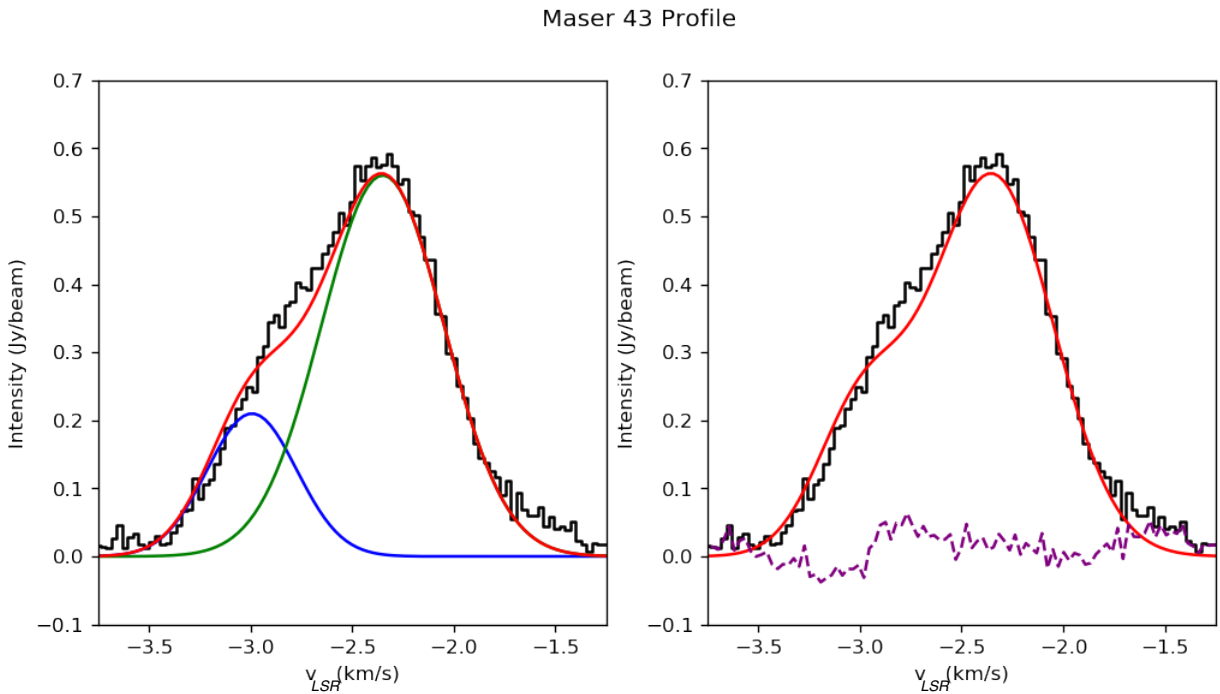


Figure 3.16: Observed profile (black histogram-like line) at 44 GHz toward DR21(OH), fitted Gaussian components (blue and green curves), sum of the fitted Gaussian components (red curve), and residuals from the fit (dashed purple curve) as described in Figure 3.4, but for maser 43 listed in Table 3.1.

Maser 48

Maser 48 is located near the center of the inner arc in the eastern lobe (Figure 3.2). Of the five masers in this inner arc, it is the strongest. Figure 3.17 shows the observed profile for this maser. It was fitted with a single Gaussian component centered at -6.183 km s^{-1} with an intensity of $12.25 \text{ Jy beam}^{-1}$, but is quite narrow with a FWHM velocity linewidth of 0.227 km s^{-1} (Table 3.1). The variability of this maser is discussed in Section 4.2.4.

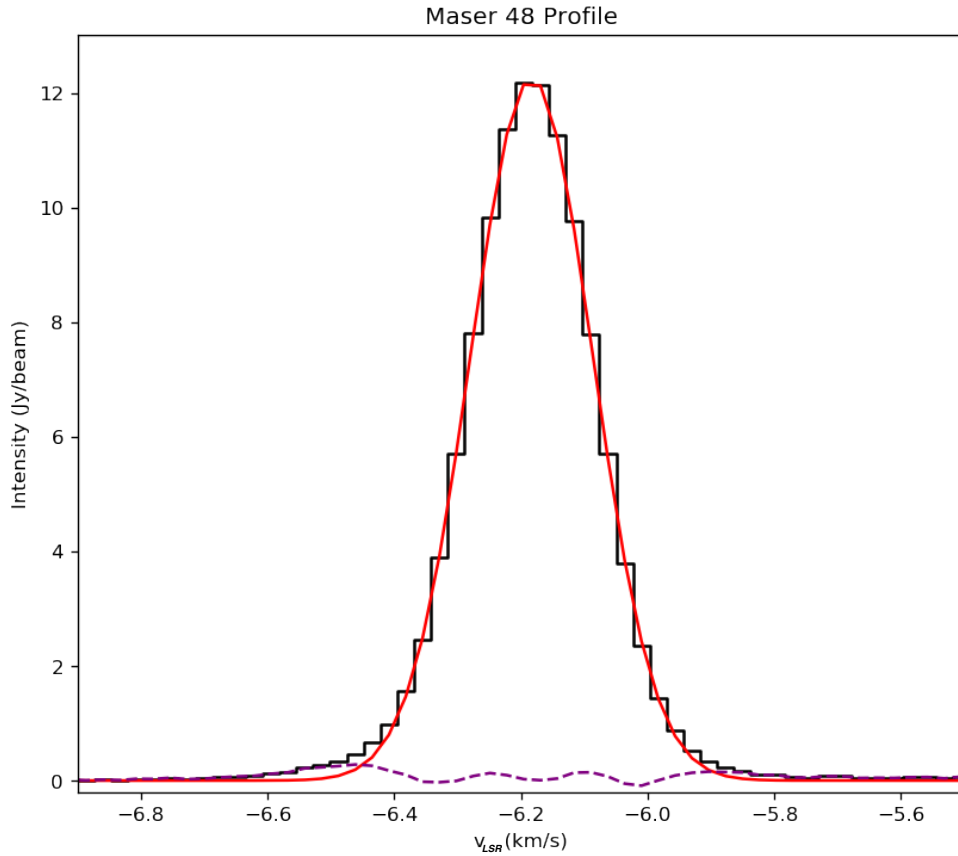


Figure 3.17: Observed profile (black histogram-like line) at 44 GHz of the Class I CH_3OH line toward DR21(OH) designated as maser 48 in Table 3.1. The profile was fitted by a single Gaussian component shown by the red curve; the dashed purple curve shows the residuals from the fit.

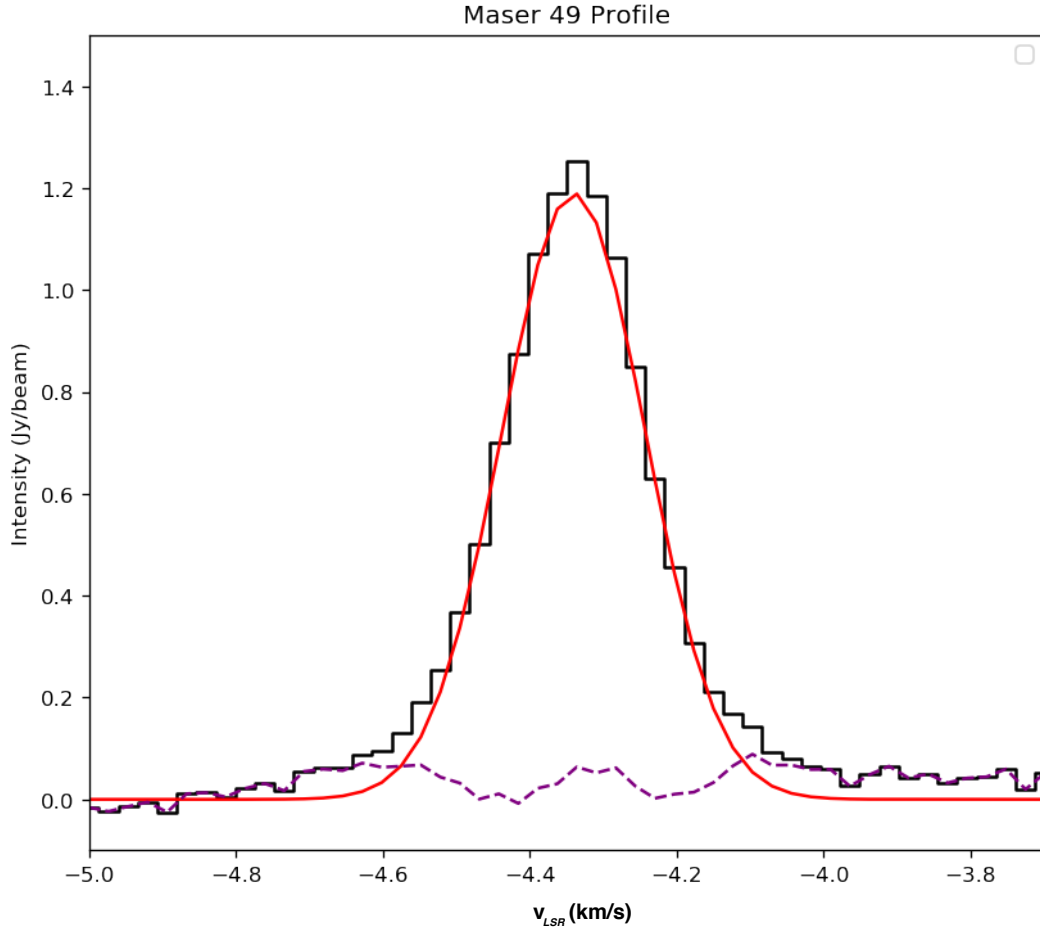


Figure 3.18: Observed profile (black histogram-like line) at 44 GHz of the Class I CH_3OH line toward DR21(OH) designated as maser 49 in Table 3.1. The profile was fitted by a single Gaussian component shown by the red curve; the dashed purple curve shows the residuals from the fit.

Maser 49

Maser 49 is located in the northern part of the outer arc in the eastern lobe (Figure 3.2). Figure 3.18 shows the observed profile for this maser. It was fitted with a single Gaussian component (Table 3.1) of intensity $1.19 \text{ Jy beam}^{-1}$ centered at -4.340 km s^{-1} that is quite narrow (FWHM velocity linewidth 0.230 km s^{-1}). The variability of this maser is discussed in Section 4.2.5.

Maser 51

Maser 51 is located in the southern part of the outer arc of the eastern lobe. The observed profile for this maser was fitted with two Gaussian components (Figure 3.19). The stronger component with intensity $4.60 \text{ Jy beam}^{-1}$ is narrower (FWHM velocity linewidth 0.345 km s^{-1}) and centered at -5.181 km s^{-1} , whereas the lower intensity component ($4.14 \text{ Jy beam}^{-1}$) is slightly broader (FWHM velocity linewidth 0.430 km s^{-1}) and is centered at -5.515 km s^{-1} .

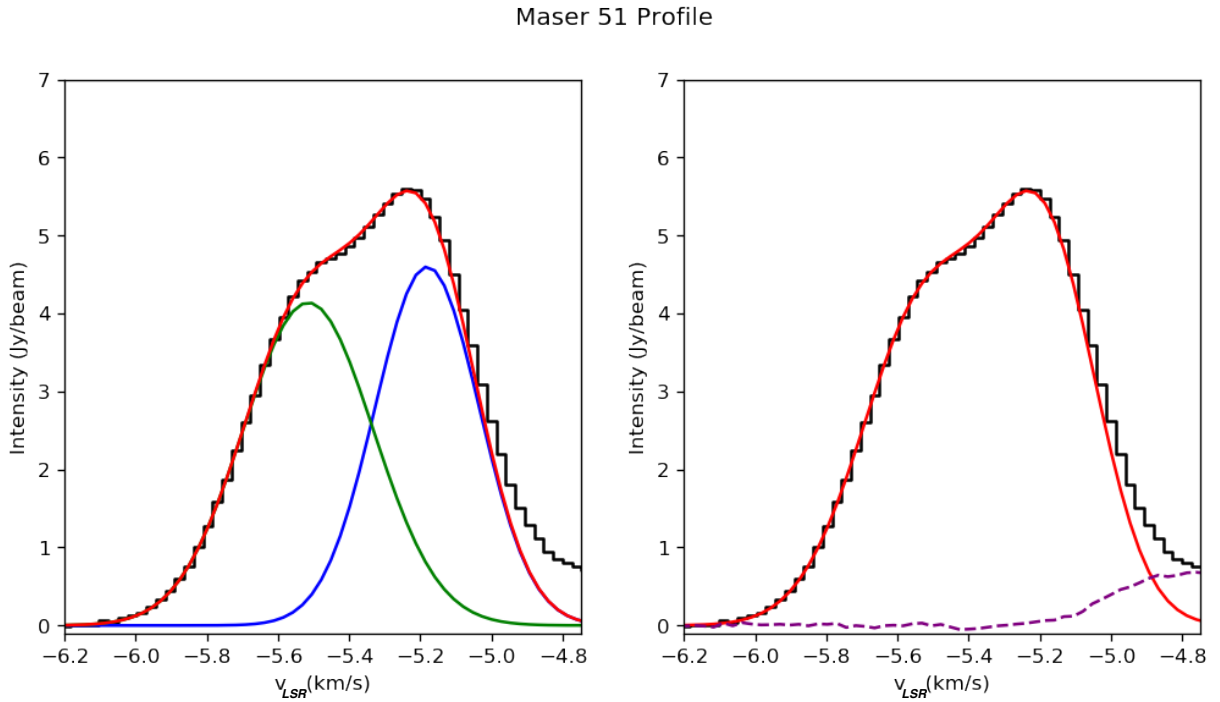


Figure 3.19: Observed profile (black histogram-like line) at 44 GHz toward DR21(OH), fitted Gaussian components (blue and green curves), sum of the fitted Gaussian components (red curve), and residuals from the fit (dashed purple curve) as described in Figure 3.4, but for maser 51 listed in Table 3.1.

Maser 53

Maser 53 is located in the outer arc of the eastern lobe, about $4''$ to the east of maser 49. Figure 3.20 shows the observed profile for this maser. It was fitted with a single Gaussian component centered at -3.183 km s^{-1} (Table 3.1) which is high in intensity ($16.56 \text{ Jy beam}^{-1}$) but quite narrow (FWHM velocity linewidth 0.425 km s^{-1}). The variability of this maser is discussed in Section 4.2.5.

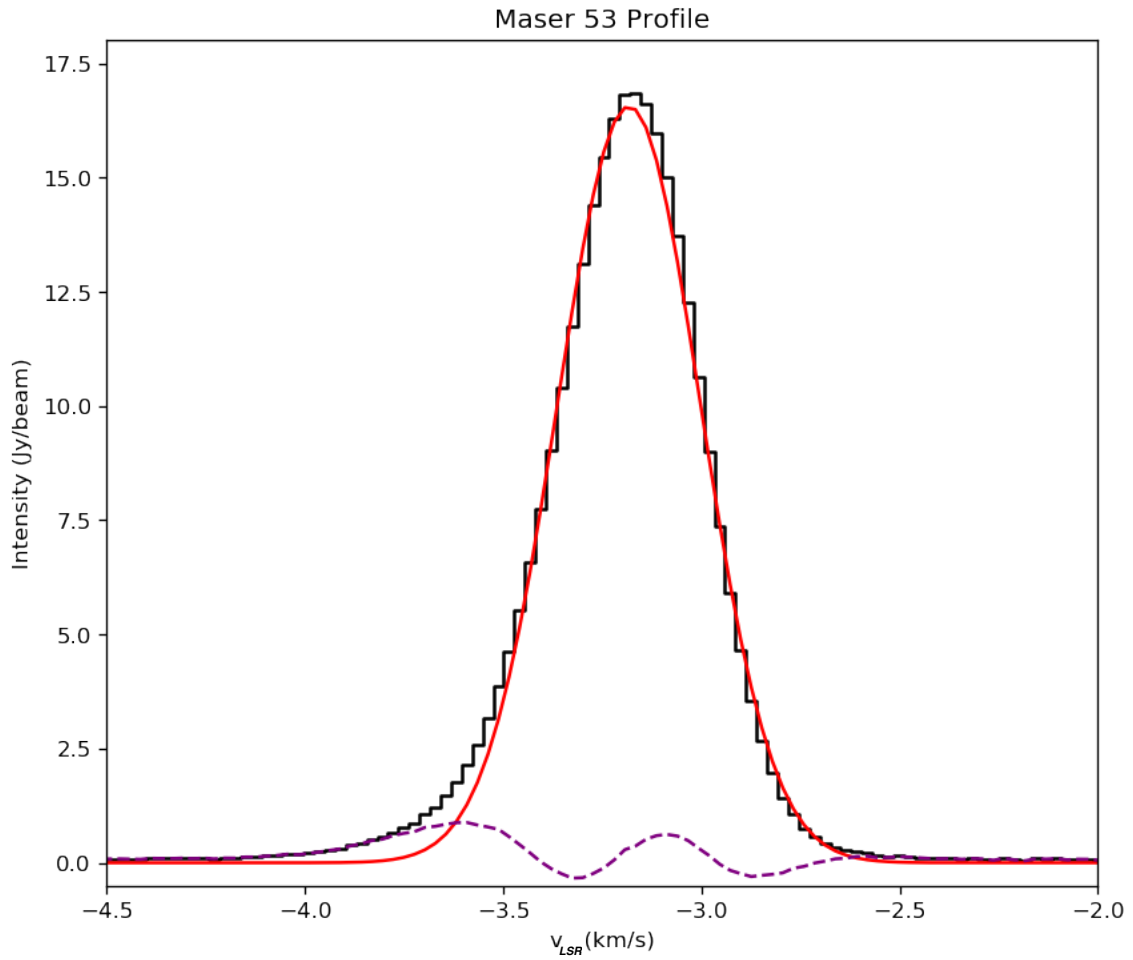


Figure 3.20: Observed profile (black histogram-like line) at 44 GHz of the Class I CH_3OH line toward DR21(OH) designated as maser 53 in Table 3.1. The profile was fitted by a single Gaussian component shown by the red curve; the dashed purple curve shows the residuals from the fit.

Maser 56

Maser 56 is located in the outer arc of the eastern lobe, about $1.2''$ to the south of maser 53 (Figure 3.2). It was fitted with two Gaussian components in velocity (Figure 3.21). The stronger component with intensity $15.03 \text{ Jy beam}^{-1}$ is slightly narrower (FWHM velocity linewidth 0.617 km s^{-1}) and centered at -5.039 km s^{-1} , whereas the lower intensity component ($2.47 \text{ Jy beam}^{-1}$) is slightly broader (FWHM velocity linewidth 0.628 km s^{-1}) and is centered at -4.326 km s^{-1} (Table 3.1).

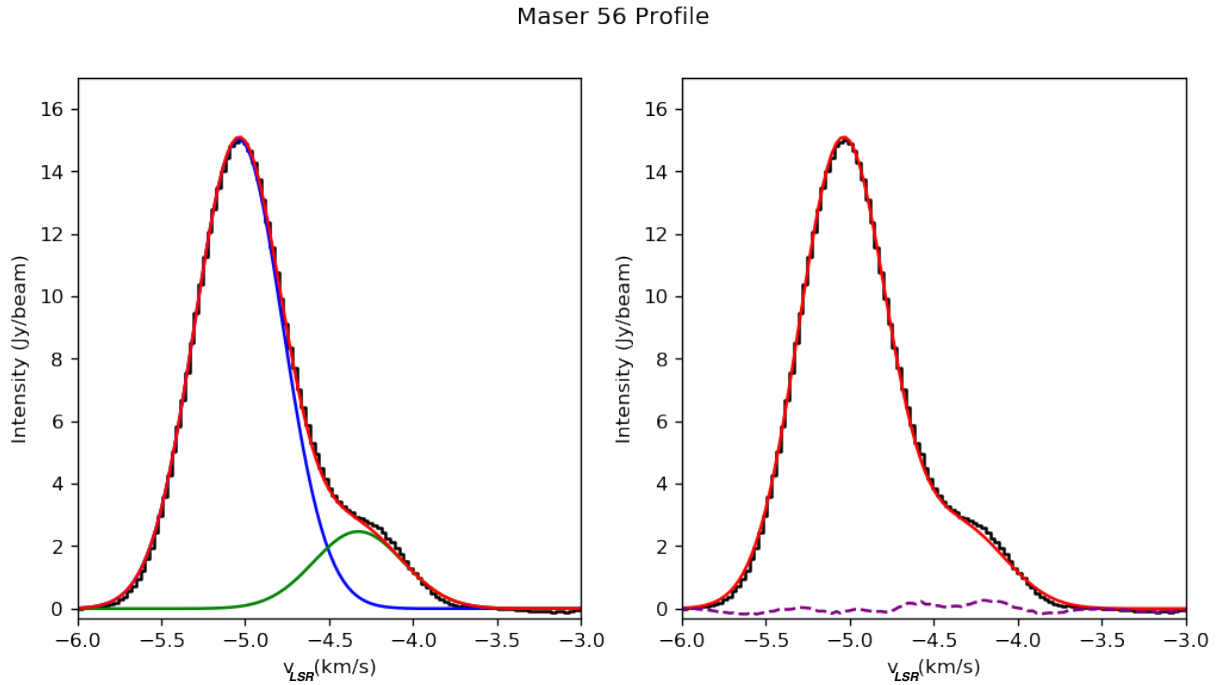


Figure 3.21: Observed profile (black histogram-like line) at 44 GHz toward DR21(OH), fitted Gaussian components (blue and green curves), sum of the fitted Gaussian components (red curve), and residuals from the fit (dashed purple curve) as described in Figure 3.4, but for maser 56 listed in Table 3.1.

3.2 Results from the 2001 Observations

Observations of Class I CH₃OH masers in DR21(OH) carried out in 2001 were reported in Araya et al. (2009). A total of 49 masers were observed. The positions of these masers, taken from Araya et al. (2009), are listed in Table 3.2. Also listed in this table is the number of the maser in the 2017 observations, taken from Table 3.1. Such correspondence was established by direct comparison of the positions (in RA and Dec.) of the masers in the 2001 and 2017 observations. Comparison of positions was made by allowing for differences of 0.6'' in RA and Dec. between the maser positions in these two epochs, that is, within the beam width of the observations in each epoch.

3.3 Results from the 2012 Observations

Observations of a subset of the Class I CH₃OH masers in DR21(OH) were carried out in 2012 with the aim of measuring the Zeeman effect (Momjian & Sarma, 2017). These observations have the same angular resolution and the same spectral resolution as the 2017 observations presented in Section 3.1. Due to the smaller range in frequency coverage however (1 MHz compared to 4 MHz in 2017), only 24 maser spots were observed. The positions of these masers, taken from Momjian & Sarma (2017) are listed in Table 3.3. There was a systematic offset of 0.5'' in the declination values of the 2012 observations when compared to the 2017 observations; this has been added to all declination values in Table 3.3. Also listed in this table are the corresponding numbers of the masers in the 2017 observations from Table 3.1. The center velocities of the masers observed in 2012 are in the range -2.369 km s^{-1} to 2.524 km s^{-1} . Thus, only the redshifted masers were observed in 2012.

Table 3.1: Fitted parameters of the Observed 44 GHz Class I CH₃OH Masers in DR21(OH)

(1)	(2)	(3)	(4)	(5)	(6)
Maser #	R.A. (J2000)	Decl. (J2000)	Peak Intensity (Jy beam ⁻¹)	Center Velocity (km s ⁻¹)	Velocity Width (km s ⁻¹)
1	20 38 58.49	42 23 16.6	1.10 ± 0.02	-2.207 ± 0.003	0.312 ± 0.008
2a	20 38 58.66	42 22 22.0	0.84 ± 0.02	-1.267 ± 0.003	0.362 ± 0.008
2b	0.56 ± 0.01	0.729 ± 0.006	0.499 ± 0.015
3a	20 38 58.90	42 22 27.2	0.45 ± 0.01	-5.095 ± 0.017	0.599 ± 0.029
3b	0.27 ± 0.02	-5.802 ± 0.025	0.644 ± 0.084
3c	0.17 ± 0.01	-6.664 ± 0.061	0.962 ± 0.119
4a	20 38 59.24	42 22 48.8	197.64 ± 8.91	0.850 ± 0.002	0.368 ± 0.004
4b	75.69 ± 5.00	0.591 ± 0.022	0.518 ± 0.021
5	20 38 59.29	42 22 49.6	13.65 ± 0.13	1.140 ± 0.001	0.312 ± 0.004
6a	20 38 59.31	42 22 47.5	6.60 ± 0.55	-0.887 ± 0.004	0.389 ± 0.009
6b	0.67 ± 0.27	-1.188 ± 0.180	0.592 ± 0.192
7	20 38 59.33	42 22 47.2	5.52 ± 0.06	-1.019 ± 0.002	0.344 ± 0.005
8	20 38 59.39	42 22 46.8	0.72 ± 0.01	-1.416 ± 0.003	0.355 ± 0.008
9	20 38 59.52	42 23 5.2	3.48 ± 0.02	-0.833 ± 0.001	0.241 ± 0.001
10	20 38 59.63	42 22 47.1	0.14 ± 0.01	-0.347 ± 0.011	0.533 ± 0.028

Continued on next page

Table 3.1 ... *Continued from previous page*

(1)	(2)	(3)	(4)	(5)	(6)
Maser #	R.A. (J2000)	Decl. (J2000)	Peak Intensity (Jy beam ⁻¹)	Center Velocity (km s ⁻¹)	Velocity Width (km s ⁻¹)
11	20 38 59.70	42 22 42.2	0.27 ± 0.01	-0.112 ± 0.050	0.486 ± 0.015
12a	20 38 59.71	42 23 16.0	0.73 ± 0.01	-0.926 ± 0.008	0.585 ± 0.019
12b	0.51 ± 0.02	-0.350 ± 0.009	0.386 ± 0.018
13	20 38 59.72	42 22 45.8	0.45 ± 0.01	-0.078 ± 0.004	0.541 ± 0.011
14	20 38 59.72	42 22 47.6	0.31 ± 0.01	0.142 ± 0.004	0.193 ± 0.009
15a	20 38 59.72	42 22 49.5	1.01 ± 0.15	0.216 ± 0.003	0.225 ± 0.014
15b	0.45 ± 0.07	0.015 ± 0.053	0.408 ± 0.066
16	20 38 59.75	42 22 45.3	0.57 ± 0.01	-0.265 ± 0.004	0.362 ± 0.010
17	20 38 59.83	42 22 50.0	0.19 ± 0.01	-1.038 ± 0.010	0.555 ± 0.027
18a	20 38 59.85	42 22 45.9	12.01 ± 0.43	-0.214 ± 0.001	0.205 ± 0.003
18b	2.78 ± 0.42	-0.471 ± 0.007	0.263 ± 0.015
18c	2.40 ± 0.25	-0.074 ± 0.051	0.554 ± 0.068
19	20 38 59.89	42 22 45.2	18.42 ± 0.44	0.337 ± 0.004	0.226 ± 0.005
20	20 38 59.90	42 22 44.9	16.27 ± 0.33	0.561 ± 0.002	0.203 ± 0.002
21	20 38 59.90	42 22 50.2	0.19 ± 0.01	-0.799 ± 0.010	0.489 ± 0.028
22	20 38 59.91	42 22 47.8	0.17 ± 0.00	-0.660 ± 0.009	0.680 ± 0.023

Continued on next page

Table 3.1 ... *Continued from previous page*

(1)	(2)	(3)	(4)	(5)	(6)
Maser #	R.A. (J2000)	Decl. (J2000)	Peak Intensity (Jy beam ⁻¹)	Center Velocity (km s ⁻¹)	Velocity Width (km s ⁻¹)
23	20 38 59.98	42 22 35.1	0.48 ± 0.01	-1.830 ± 0.002	0.253 ± 0.006
24	20 39 0.01	42 22 47.0	0.16 ± 0.01	-1.658 ± 0.010	0.574 ± 0.027
25a	20 39 0.06	42 22 44.5	1.67 ± 0.03	-8.650 ± 0.001	0.326 ± 0.004
25b	0.58 ± 0.03	-8.490 ± 0.010	0.630 ± 0.011
26	20 39 0.09	42 22 43.6	1.43 ± 0.01	-5.112 ± 0.002	0.353 ± 0.004
27a	20 39 0.13	42 22 48.8	0.09 ± 0.02	-2.463 ± 0.158	0.812 ± 0.283
27b	0.11 ± 0.05	-1.973 ± 0.037	0.487 ± 0.082
28a	20 39 0.14	42 22 47.1	1.07 ± 0.03	-1.321 ± 0.006	0.562 ± 0.009
28b	0.41 ± 0.01	-0.720 ± 0.026	0.791 ± 0.042
29	20 39 0.15	42 22 47.7	10.07 ± 0.10	-1.445 ± 0.002	0.395 ± 0.005
30a	20 39 0.23	42 22 45.9	277.66 ± 3.89	0.465 ± 0.002	0.279 ± 0.003
30b	57.42 ± 2.75	0.205 ± 0.013	0.316 ± 0.018
31a	20 39 0.25	42 22 46.4	3.59 ± 0.12	0.323 ± 0.007	0.472 ± 0.006
31b	0.83 ± 0.02	1.182 ± 0.008	0.570 ± 0.021
32	20 39 0.25	42 22 47.4	9.85 ± 0.22	0.106 ± 0.001	0.340 ± 0.003
33a	20 39 0.29	42 22 47.0	1.23 ± 0.01	-2.099 ± 0.002	0.366 ± 0.005

Continued on next page

Table 3.1 ... *Continued from previous page*

(1)	(2)	(3)	(4)	(5)	(6)
Maser #	R.A. (J2000)	Decl. (J2000)	Peak Intensity (Jy beam ⁻¹)	Center Velocity (km s ⁻¹)	Velocity Width (km s ⁻¹)
33b	0.28 ± 0.01	-2.786 ± 0.009	0.417 ± 0.023
34	20 39 0.32	42 22 48.4	1.10 ± 0.02	-0.046 ± 0.005	0.451 ± 0.012
35a	20 39 0.46	42 22 46.3	0.13 ± 0.00	-2.509 ± 0.019	1.008 ± 0.050
35b	0.12 ± 0.01	-0.611 ± 0.027	1.587 ± 0.098
36a	20 39 0.52	42 22 47.6	1.60 ± 0.05	2.561 ± 0.010	0.398 ± 0.015
36b	1.23 ± 0.06	2.137 ± 0.013	0.396 ± 0.051
36c	0.55 ± 0.02	1.357 ± 0.008	0.289 ± 0.016
36d	2.37 ± 0.90	1.774 ± 0.008	0.344 ± 0.013
37a	20 39 0.59	42 22 44.9	0.11 ± 0.01	-2.303 ± 0.031	0.803 ± 0.065
37b	0.08 ± 0.01	-1.490 ± 0.035	0.640 ± 0.077
38	20 39 1.02	42 22 17.6	0.38 ± 0.01	-3.182 ± 0.007	0.377 ± 0.017
39	20 39 1.02	42 22 41.6	0.66 ± 0.01	-1.049 ± 0.002	0.469 ± 0.006
40	20 39 1.05	42 22 41.5	0.28 ± 0.01	-1.175 ± 0.007	0.491 ± 0.017
41	20 39 1.07	42 22 00.9	1.56 ± 0.05	-1.811 ± 0.005	0.358 ± 0.013
42a	20 39 1.14	42 22 06.7	1.07 ± 0.02	-1.034 ± 0.005	0.750 ± 0.016
42b	0.54 ± 0.03	-3.549 ± 0.007	0.276 ± 0.016

Continued on next page

Table 3.1 ... *Continued from previous page*

(1)	(2)	(3)	(4)	(5)	(6)
Maser #	R.A. (J2000)	Decl. (J2000)	Peak Intensity (Jy beam ⁻¹)	Center Velocity (km s ⁻¹)	Velocity Width (km s ⁻¹)
43a	20 39 1.21	42 22 41.0	0.56 ± 0.01	-2.349 ± 0.011	0.711 ± 0.018
43b	0.21 ± 0.01	-2.933 ± 0.019	0.519 ± 0.030
44	20 39 1.45	42 23 06.2	0.10 ± 0.01	-1.750 ± 0.033	2.148 ± 0.121
45	20 39 1.47	42 22 07.5	0.18 ± 0.02	-4.153 ± 0.033	0.788 ± 0.098
46	20 39 1.48	42 22 45.1	1.22 ± 0.01	-2.832 ± 0.003	0.613 ± 0.009
47a	20 39 1.49	42 22 40.8	10.20 ± 0.09	-4.380 ± 0.002	0.387 ± 0.006
47b	1.85 ± 0.46	-4.795 ± 0.010	0.196 ± 0.033
48	20 39 1.64	42 22 43.3	12.25 ± 0.04	-6.183 ± 0.001	0.227 ± 0.001
49	20 39 1.68	42 22 45.2	1.19 ± 0.01	-4.340 ± 0.001	0.230 ± 0.003
50	20 39 1.75	42 22 45.3	0.14 ± 0.01	-3.186 ± 0.013	0.627 ± 0.033
51a	20 39 1.99	42 22 40.8	4.60 ± 0.16	-5.181 ± 0.003	0.345 ± 0.009
51b	4.14 ± 0.07	-5.515 ± 0.006	0.430 ± 0.007
52	20 39 1.99	42 22 41.1	5.07 ± 0.02	-4.176 ± 0.001	0.460 ± 0.003
53	20 39 2.05	42 22 45.2	16.56 ± 0.97	-3.183 ± 0.001	0.425 ± 0.003
54	20 39 2.18	42 22 43.3	0.65 ± 0.02	-3.851 ± 0.006	0.403 ± 0.014
55	20 39 2.20	42 22 42.4	4.28 ± 0.02	-3.228 ± 0.002	0.305 ± 0.003

Continued on next page

Table 3.1 ... *Continued from previous page*

(1)	(2)	(3)	(4)	(5)	(6)
Maser #	R.A. (J2000)	Decl. (J2000)	Peak Intensity (Jy beam ⁻¹)	Center Velocity (km s ⁻¹)	Velocity Width (km s ⁻¹)
56a	20 39 2.21	42 22 44.0	15.03 ± 0.03	-5.039 ± 0.001	0.617 ± 0.002
56b	2.47 ± 0.03	-4.326 ± 0.006	0.628 ± 0.014
57	20 39 2.25	42 22 43.0	0.56 ± 0.01	-4.097 ± 0.006	0.573 ± 0.014

Table 3.2: Observed Masers in DR21(OH) from Araya et al. (2009)

(1)	(2)	(3)	(4)
Araya	R.A.	Decl.	Corresponding
Maser ID	(J2000)	(J2000)	2017 maser
2001-1	20 38 58.68	42 22 22.1	2
2001-2	20 38 58.92	42 22 27.2	3
2001-3	20 38 59.29	42 22 48.8	4
2001-4	20 38 59.32	42 22 49.6	5
2001-5	20 38 59.35	42 22 47.4	6
2001-6	20 38 59.56	42 23 5.3	9
2001-7	20 38 59.64	42 22 47.2	10
2001-8	20 38 59.72	42 22 49.6	15
2001-9	20 38 59.73	42 23 16.2	12
2001-10	20 38 59.73	42 22 47.6	14
2001-11	20 38 59.76	42 22 45.5	16
2001-12	20 38 59.83	42 22 50.1	17
2001-13	20 38 59.89	42 22 46.0	18
2001-14	20 38 59.92	42 22 47.9	22
2001-15	20 38 59.92	42 22 50.3	21
2001-16	20 38 59.93	42 22 45.0	20
2001-17	20 38 59.99	42 22 35.2	23
2001-18	20 39 0.08	42 22 47.1	24
2001-19	20 39 0.09	42 22 44.7	25
2001-20	20 39 0.12	42 22 43.7	26
2001-21	20 39 0.13	42 22 47.1	28
2001-22	20 39 0.14	42 22 48.8	27
2001-23	20 39 0.19	42 22 47.7	29
2001-24	20 39 0.26	42 22 46.0	30

Continued on next page

Table 3.2 ··· *Continued from previous page*

(1)	(2)	(3)	(4)
Araya	R.A.	Decl.	Corresponding
Maser ID	(J2000)	(J2000)	2017 maser
2001–25	20 39 0.29	42 22 47.4	32
2001–26	20 39 0.33	42 22 48.5	34
2001–27	20 39 0.49	42 22 46.3	35
2001–28	20 39 0.55	42 22 47.7	36
2001–29	20 39 0.60	42 22 45.0	37
2001–30	20 39 1.05	42 22 41.6	40
2001–31	20 39 1.05	42 22 17.6	38
2001–32	20 39 1.09	42 22 1.0	41
2001–33	20 39 1.17	42 22 6.8	42
2001–34	20 39 1.18	42 22 6.8	42
2001–35	20 39 1.22	42 22 41.2	43
2001–36	20 39 1.47	42 23 6.3	44
2001–37	20 39 1.48	42 22 7.6	45
2001–38	20 39 1.50	42 22 45.2	46
2001–39	20 39 1.51	42 22 40.8	47
2001–40	20 39 1.54	42 22 2.8	None
2001–41	20 39 1.67	42 22 43.4	48
2001–42	20 39 1.70	42 22 45.2	49
2001–43	20 39 1.76	42 22 45.3	50
2001–44	20 39 2.02	42 22 41.2	52
2001–45	20 39 2.02	42 22 40.8	51
2001–46	20 39 2.08	42 22 45.2	53
2001–47	20 39 2.21	42 22 43.4	54
2001–48	20 39 2.22	42 22 42.6	55
2001–49	20 39 2.24	42 22 44.0	56

Table 3.3: Observed Masers in DR21(OH) from Momjian & Sarma (2017)

(1)	(2)	(3)	(4)
MS	R.A.	Decl.	Corresponding
Maser ID	(J2000)	(J2000)	2017 maser
2012-1a	20 38 59.25	42 22 48.7	4a
2012-1b	4b
2012-2	20 38 59.29	42 22 47.5	6a
2012-3	20 38 59.31	42 22 49.6	5
2012-4	20 38 59.33	42 22 47.3	7
2012-5	20 38 59.70	42 22 42.2	11
2012-6	20 38 59.71	42 22 45.8	13
2012-7a	20 38 59.71	42 22 49.6	15a
2012-7b	15b
2012-8	20 38 59.76	42 22 45.2	16
2012-9	20 38 59.85	42 22 45.9	18a
2012-10	20 38 59.85	42 22 46.2	18b
2012-11	20 38 59.89	42 22 45.4	19
2012-12	20 38 59.91	42 22 45.0	20
2012-13	20 38 59.96	42 22 35.2	23
2012-14	20 39 0.15	42 22 47.8	29
2012-15a	20 39 0.23	42 22 45.9	30a
2012-15b	30b
2012-16	20 39 0.25	42 22 47.3	32
2012-17a	20 39 0.25	42 22 46.5	31b
2012-17b	31a
2012-18	20 39 0.30	42 22 47.1	33a
2012-19	20 39 0.33	42 22 48.3	34

Continued on next page

Table 3.3 ... *Continued from previous page*

(1)	(2)	(3)	(4)
MS	R.A.	Decl.	Corresponding
Maser ID	(J2000)	(J2000)	2017 maser
2012–20	20 39 0.51	42 22 47.6	36c
2012–21a	20 39 0.53	42 22 47.6	36a
2012–21b	36b
2012–22	20 39 0.52	42 22 47.6	36d
2012–23	20 39 1.01	42 22 41.6	39
2012–24	20 39 1.20	42 22 41.0	43

CHAPTER 4

Discussion

The central aim of this thesis is to look for variability in 44 GHz Class I CH₃OH masers by comparing observations taken in 2017 with those taken in 2001 and 2012. This chapter will begin with a discussion of the maser distribution across all three epochs (Section 4.1). The variability of masers will be discussed in Section 4.2, and a discussion on the likely causes of these variations will be presented in Section 4.3.

4.1 Maser Distribution

A total of 57 masers were detected in the 2017 observations reported in this thesis. All 24 of the masers observed in 2012 and published in Momjian & Sarma (2017) were also detected in these 2017 observations. It is worth noting again here that only a reduced number of masers were observed in 2012 due to the narrower bandwidth available with a channel spacing of 0.026 km s^{-1} during those observations. Araya et al. (2009) reported a total of 49 masers in their 2001 observations. Only one of these was not detected in the 2017 observations. Of the other 48 masers, maser 2001-5 (in Table 3.2) could be masers 6 and 7 in the 2017 observations (Table 3.1); Araya et al. (2009) might have observed these two as only one maser due to their lower velocity resolution. Likewise, maser 2001-16 in Araya et al. (2009) could be masers 19 and 20 in the 2017 observations, which might again have showed up as one maser due to the lower velocity resolution in the 2001 data. The remaining seven masers in the 2017 data are low intensity masers that would have been significantly less prominent in the lower velocity resolution of the 2001 observations. In principle, though, it is possible that all nine of these could be new masers that did not exist

in 2001. Nevertheless, it is clear that Class I CH_3OH masers are stable entities because almost 90% of the masers have appeared at the same position over more than a 15-yr period from 2001 to 2017.

As shown in Figure 3.2, the Class I CH_3OH masers at 44 GHz in DR21(OH) are distributed in a western lobe and an eastern lobe, with two arcs of masers in each lobe. This is consistent with the distribution observed by Araya et al. (2009) in their 2001 data. Figure 4.1 shows the distribution of the masers in this double arc feature in each lobe across all three epochs, 2001, 2012, and 2017. This figure highlights the stability of the overall distribution over the 2001 to 2017 period. As noted above, almost 90% of masers are present at nearly the same position during this period.

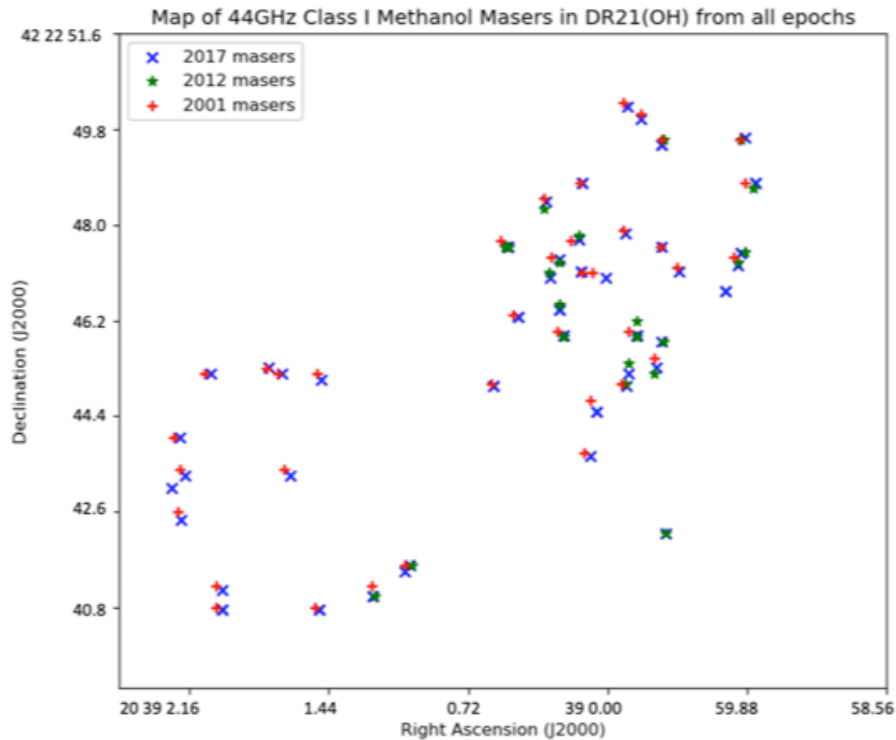


Figure 4.1: Figure showing the locations of all the masers across all three epochs. The red crosses represent the masers observed by Araya et al. (2009) in 2001, the green stars represent the masers observed by Momjian & Sarma (2017) in 2012, and the blue x's represent the masers observed in 2017.

A notable difference between the 2001 and 2012 data is in the locations of the strongest masers. Between 2001 and 2012, the two strongest masers in the field flipped in strength, so that the brightest maser in 2001 became the second brightest maser in 2012, and vice versa. In 2001, the strongest maser was located in the outer arc of the western lobe (currently at the location of maser 4 in Figure 3.2). The second strongest maser was located about $10''$ away in the inner arc of the eastern lobe (currently at the location of maser 30 in Figure 3.2). However, in 2012, the opposite is true: the strongest maser now resides in the inner arc of the western lobe (currently at the location of maser 30 in Figure 3.2) while the second strongest maser is located in the outer arc (currently at the location of maser 4 in Figure 3.2). This has remained unchanged from the 2012 to 2017 data; maser 30 in the inner arc is the strongest, and maser 4 in the outer arc is the second strongest maser.

4.2 Maser Variability

The discussion in the previous section has established that while the masers themselves have been stable entities over more than a 15 yr period between 2001 and 2017, there have likely been changes in the intensities of individual masers. Direct comparisons between the 2001 and 2017 data are difficult due to the difference in velocity resolution (0.7 km s^{-1} vs. 0.0266 km s^{-1} respectively). An examination of the qualitative trends (i.e., whether intensities have increased or decreased) between these epochs can be done by smoothing the higher velocity resolution data down to that of the 2001 dataset. The 2017 dataset was velocity-smoothed to examine in this manner the increase or decrease in the intensities between 2001 and 2017. The 2012 dataset was also velocity-smoothed to investigate the changes in intensity for the two strongest masers from 2001 to 2012. The smoothing in velocity was done using the AIPS task XSMTH; more details are in Section 4.2.1.

Direct comparisons can be made between the 2012 and 2017 data, because they were obtained with about the same angular and velocity resolution. To account for errors

in the calibrator used to set the flux in the source, it is common practice to ignore any variations below the 10% level. I adopt this standard, and report a variation only if it is larger than 10%. Of the 24 masers found in the 2012 data, 17 masers varied in intensity by more than 10%. Out of these 17 masers, only three increased in intensity from 2012 to 2017; they are maser 33, maser 30b (the weaker velocity component of maser 30), and maser 36b (one of the four velocity components of maser 36); maser numbers refer to the listing in Table 3.1. The other 14 of these 17 masers decreased in intensity by more than 10% from 2012 to 2017; they are 5, 7, 11, 13, 16, 18a, 18b, 23, 30a, 31, 32, 36a, 36c, 36d, 39, and 43. The two velocity components of maser 18 listed as 18a and 18b in Table 3.1 were registered in 2012 as two nearby but separate masers, and the four velocity components of maser 36 were registered in 2012 as three separate masers (Table 3.3). Changes in the two strongest masers are discussed in more detail in Section 4.2.1, and changes in several other masers in each of the two arcs of the western and eastern lobes are discussed in Section 4.2.2 through Section 4.2.5.

4.2.1 The two strongest masers: Maser 4 and Maser 30

The two strongest Class I CH₃OH masers at 44 GHz toward DR21(OH) displayed interesting behavior. As noted above in Section 4.1, the two strongest masers flipped between 2001 and 2012. Maser 30 is the brightest, and maser 4 is the second brightest maser in the field in the 2017 and 2012 data. Maser 30 is located in the inner arc of the western lobe, and maser 4 is located in its outer arc (see Table 3.1 and Figure 3.1). In 2001, however, the opposite was true; maser 4 was brighter than maser 30. The reversal in rank did not happen because one increased in intensity while the other decreased or remained the same, however. Instead, both masers went up in intensity from 2001 to 2012. This was established by comparing the intensities of these two masers in the velocity-smoothed data of 2012 with the 2001 maser intensities from Araya et al. (2009).

The velocity smoothing of the 2012 data was done using the task XSMTH in AIPS. The parameter NPOINTS in XSMTH was chosen to give a similar velocity resolution after the smoothing as that of Araya et al. (2009) while at the same time ensuring that the intensities of masers 30 and 4 would be roughly in the same ratio after the smoothing as before. The ratio of the intensity of maser 30 to that of maser 4 after the velocity smoothing was 1.3. Before the smoothing (that is, in the 2012 data with higher velocity resolution), the stronger component of maser 30 was 1.5 times brighter than that of maser 4. There is a slight difference between the two ratios (1.3 *vs.* 1.5), likely because at the higher velocity resolution, maser 4 has a second lower intensity component that is still stronger than the second component of maser 30. Upon comparing the intensities of masers 4 and 30 in the velocity-smoothed data of 2012 to the intensities in the 2001 data, it was found that maser 4 became 1.6 times brighter from 2001 to 2012, but maser 30 became 7.7 times brighter during that same period. Thus, maser 30 went through a much larger increase in intensity from 2001 to 2012 compared to maser 4.

Next, both the 2012 and 2017 observations have similar angular resolution and the same velocity resolution. Therefore, direct comparisons can be made between these two epochs. Neither the stronger nor the weaker component of maser 4 varied above the 10% level between 2012 and 2017. On the other hand, the stronger component of maser 30 showed a marginal decrease of 14% from 2012 to 2017, whereas the weaker component showed a significant increase of 29% from $44.30 \text{ Jy beam}^{-1}$ to $57.42 \text{ Jy beam}^{-1}$. One interpretation of these numbers is that maser 4 in the outer arc of the western lobe has reached a quieter stage after 2012, whereas changes are still going on in maser 30 in the inner arc of the western lobe. Also of interest is that the stronger component of maser 30 is 1.4 times brighter than the stronger component of maser 4 in 2017, roughly the same relation they had between their intensities in 2012.

4.2.2 Masers in the outer arc of the western lobe

There are 11 masers in the outer arc of the western lobe (Table 4.1), of which maser 4 has already been discussed in Section 4.2.1 above. Of the rest, maser 5 has intensity $13.65 \text{ Jy beam}^{-1}$, and masers 6, 7, 15, 34 and 36 have intensities 1-10 Jy beam^{-1} . Maser 5 is located to the north of maser 4, almost at the head of the bowshock delineated by the outer arc in the western lobe. Masers 5, 6, 15, 34, and 36 went up in intensity from 2001 to 2017; this trend was obtained by comparing the intensity observed in 2001 with the intensity in the velocity-smoothed dataset for 2017. Direct comparison of the 2012 and 2017 data showed that practically all of these masers either decreased in intensity from 2012 to 2017, or remained unchanged at the 10% level. For example, maser 5 decreased by 16.4% from $16.33 \text{ Jy beam}^{-1}$ in 2012 to $13.65 \text{ Jy beam}^{-1}$ in 2017. The only exception was one of the four components of maser 36, which increased in intensity by 12.8% from $1.09 \text{ Jy beam}^{-1}$ to $1.23 \text{ Jy beam}^{-1}$, although only marginally above the 10% level. Since masers 5, 6, 15, 34, and 36 went up in intensity from 2001 to 2017, but decreased or stayed the same from 2012 to 2017, they must have increased in intensity from 2001 to 2012. This conclusion was verified explicitly for masers 5 and 6 by comparing the intensity observed in 2001 to the velocity-smoothed dataset for 2012.

Table 4.1: Maser spots in arcs and lobes

Location	Total	Masers
Outer arc, western lobe	11	4, 5, 6, 7, 8, 15, 17, 21, 27, 34, 36
Inner arc, western lobe	20	10, 11, 13, 14, 16, 18, 19, 20, 22, 24, 25, 26, 28, 29, 30, 31, 32, 33, 35, 37
Inner arc, eastern lobe	5	39, 40, 43, 46, 48
Outer arc, eastern lobe	10	47, 49, 50, 51, 52, 53, 54, 55, 56, 57

Note: Maser numbers refer to the listing in Table 3.1.

Masers 6, 7, and 8 are of interest for additional reasons. Maser 6 appears to have picked up a second and weaker component in 2017 that was not observed in 2012; it has intensity $0.67 \text{ Jy beam}^{-1}$ and is centered at -1.188 km s^{-1} . Maser 7 was not observed in 2001, although it is possible that masers 6 and 7 could have been observed as maser 2001-5 due to the lower velocity resolution of the 2001 observations. Maser 7 went down by 16.9% from $6.64 \text{ Jy beam}^{-1}$ in 2012 to $5.52 \text{ Jy beam}^{-1}$ in 2017, so it must have appeared at some time during the period 2001-2012. Finally, maser 8 was not detected in 2001, and was not reported in Momjian & Sarma (2017). A reexamination of the 2012 data showed a source with intensity $\sim 0.8 \text{ Jy beam}^{-1}$ (and a second component lower than the 0.3 Jy beam^{-1} value that was adopted as the nominal detection limit for masers in the 2012 observations) at the RA and Dec listed for maser 8 in Table 3.1. Thus, maser 8 must have appeared sometime between 2001 and 2012. Its stronger component remained unchanged at the 10% level from 2012 to 2017, whereas its weaker component increased in intensity.

Also of interest is maser 36, which was fitted with four Gaussian components. Two of these, component 36a and components 36b, were detected as maser 2012-21a and maser 2012-21b respectively in the observations taken in 2012. The other two, component 36c and component 36d, were detected as maser 2012-20 and maser 2012-22 respectively. Direct comparison of the 2012 and 2017 datasets shows that three of these components, 36a, 36c, and 36d, decreased in intensity from 2012 to 2017, but one component, 36b, increased by 12.8% from $1.09 \text{ Jy beam}^{-1}$ to $1.23 \text{ Jy beam}^{-1}$ in 2017.

In summary, all the prominent masers in the outer arc of the western lobe exhibit variability over a 15-year period. In general, intensities appear to have increased from 2001 to 2012, then gone down or stayed the same from 2012 to 2017 for most of these masers.

4.2.3 Masers in the inner arc of the western lobe

There are 20 masers in the inner arc of the western lobe; they are listed in Table 4.1. Of these, maser 30 has already been discussed in Section 4.2.1. Of the rest, masers 18, 19, 20, and 29 have intensities between 10-20 Jy beam⁻¹, masers 25, 26, 28, 31, 32, and 33 have intensities between 1-10 Jy beam⁻¹, and the rest have intensities < 1 Jy beam⁻¹. Masers 11, 13, 31, and 33 were not present in 2001 but were observed in 2012, and masers 19 and 20 may have been reported as one maser in 2001. For the 15 masers that were present both in 2001 and 2017 (including maser 30 already discussed in Section 4.2.1), the intensity increased for all but three masers. The three exceptions are maser 24 which went down in intensity from 2001 to 2017, and masers 14 and 37 which showed no changes above the 10% level. These trends were obtained by comparing the intensity observed in 2001 with the intensity of the velocity-smoothed dataset for 2017. Masers 16, 18, 29, 30, and 32 were present in all three epochs, 2001, 2012, and 2017; masers 19 and 20 were present as separate masers in 2012 and 2017, but may have been observed as one maser in 2001. Direct comparison of the 2012 and 2017 data showed that practically all of these masers, including the four listed above that were observed in 2012 but not in 2001, either decreased in intensity from 2012 to 2017, or remained unchanged at the 10% level. For example, maser 32 decreased by 16.5% from 11.79 Jy beam⁻¹ to 9.85 Jy beam⁻¹, and the stronger component of maser 31 decreased to less than half its intensity, from 7.99 Jy beam⁻¹ in 2012 to 3.59 Jy beam⁻¹ in 2017. The only two exceptions are the weaker component of maser 30 which increased by 29.6%, and maser 33a which increased from 0.9 Jy beam⁻¹ to 1.23 Jy beam⁻¹.

Masers in the inner arc of the western lobe display the same general trend revealed by masers in the outer arc. Most, with only a few exceptions, appear to have increased in intensity from 2001 to 2012, then gone down or stayed the same from 2012 to 2017. Even though I have avoided quantitative comparisons between velocity-averaged data (except for the two strongest masers), it is striking that the increases

in the inner arc appear to be more than in the outer arc. This is discussed in more detail in Section 4.3, along with its implications.

4.2.4 Masers in the inner arc of the eastern lobe

There are 5 masers in the inner arc of the eastern lobe, and they are listed in Table 4.1. Comparison of intensities in velocity-smoothed data from 2017 with intensities observed in 2001 shows that masers 40 and 43 have decreased in intensity from 2001 to 2017, whereas masers 46 and 48 have increased in intensity. Maser 39 was not observed in 2001.

Masers 39, 40, and 43 are redshifted masers, even though they are present in the eastern lobe. Although maser 40 was below the 0.3 Jy beam^{-1} detection limit imposed for the 2012 observations, masers 39 and 43 are present in the 2012 data. Maser 39 decreased by 18.5% from $0.81 \text{ Jy beam}^{-1}$ in 2012 to $0.66 \text{ Jy beam}^{-1}$ in 2017. Maser 43 decreased from $0.63 \text{ Jy beam}^{-1}$ to $0.56 \text{ Jy beam}^{-1}$, just marginally above the 10% limit. With a center velocity of -2.83 km s^{-1} , maser 46 is also redshifted, but the velocity would have been just outside the most redshifted channel imaged in 2012. Maser 48 is blueshifted and would not have been detected in 2012.

4.2.5 Masers in the outer arc of the eastern lobe

There are 10 masers in the outer arc of the eastern lobe (Table 4.1). All of these masers are blueshifted, so they were not observed in 2012. Other than one (maser 57), all of them were also observed in 2001. Comparison of the intensities of the velocity-smoothed data from 2017 with the intensities observed in 2001 showed that seven of these masers increased in intensity, and two decreased in intensity. Since no data are available from 2012 for these masers, it is not possible to say if this increase has been consistent from 2001 to 2017, or whether an increase from 2001 until 2012 was followed by a decrease, similar to the masers in the western lobe.

4.3 Reasons for maser variability

Although variability in 44 GHz Class I CH₃OH masers has been hinted at in several papers (Momjian & Sarma, 2017; Leurini et al., 2016; Kurtz et al., 2004), there has never been a dedicated attempt to investigate variability in these masers. This thesis has established that such masers vary over the long term. A theoretical model for why such variability should occur is beyond the scope of this thesis. Nevertheless, some of the processes that could cause variability in Class I CH₃OH masers are discussed qualitatively in this section.

Masers can vary due to changes in pumping or due to changes in the path length over which the signal is amplified. A change in pumping could be caused by the propagation of a shock front through the region. It is unlikely, however, that the same shock front that caused the increase in maser 30 in the inner arc of the western lobe from 2001 to 2012 has led to the increase in maser 4 in the outer arc. The distance between maser 30 and maser 4 is about 10'', equivalent to 0.07 pc (see footnote 1 in Section 3.1). To travel from the location of maser 30 to the location of maser 4 in the over 10-yr period from 2001 to 2012 would require the shock front to be traveling at an absurdly high velocity over 5000 km s⁻¹. Instead, it is likely that we are seeing an instance of episodic accretion.

Episodes of increased accretion are well known in low mass star formation, but outbursts related to such increases in accretion have only recently been found in high mass star forming regions (e.g., Caratti o Garatti et al. 2017; Brogan et al. 2019). Each episode of accretion is accompanied by an ejection event which registers as an outward-propagating shock (Caratti o Garatti et al. 2015). Such a model would imply that the increase in intensity in the masers in the outer arc of the western lobe in DR21(OH) was caused by an earlier shock related to an enhanced accretion episode. This continued to cause a modest increase in the intensity of the masers through 2012, following which they have decreased or remained largely unchanged at

the 10% level. The increase in the intensity of masers in the inner arc of the western lobe could then be ascribed to a shock front created by a more recent accretion event that reached the inner arc sometime between 2001 and 2012.

Activity in the inner arc is significantly greater than in the outer arc in the western lobe, suggesting that this model of episodic accretion outbursts is at least plausible. For example, the increase in maser intensities in the inner arc is larger than in the outer arc. In Section 4.2.1, we have seen that maser 30 in the inner arc increased by 7.7 times from 2001 to 2012, whereas maser 4 in the outer arc increased only by a 1.6 factor. For lower intensity masers, I have avoided quantitative comparisons between the velocity-averaged data of the two later epochs with the lower velocity resolution data of 2001. But, just like the increases in the two strongest masers above, masers with intensities between 1-10 Jy beam⁻¹ in the outer arc increased by 3-5 times, whereas those in the inner arc increased by 3-8 times. Moreover, only one new low intensity maser showed up in 2017 in the outer arc of the western lobe that was not present in 2001; maser 8 has intensity 0.72 Jy beam⁻¹ (Table 3.1). On the other hand, four new masers showed up in the inner arc of the western lobe in 2017 (and 2012) that were not present in 2001; masers 11 and 13 are low intensity, but maser 31a has intensity 3.59 Jy beam⁻¹, and maser 33a is 1.23 Jy beam⁻¹ in the 2017 observations (Table 3.1). The effects of such episodic accretion aren't as clear in the eastern lobe, where there no strong masers > 20 Jy beam⁻¹.

Additional support for the model of outbursts related to accretion comes from considering the time between such episodes. If we assume that methanol masers are caused by slower-moving shocks (Leurini et al. 2016) and use a shock velocity of 20 km s⁻¹, then it would take about 3500 yr for a shock to propagate from the position of maser 30 in the inner arc to maser 4 in the outer arc. So the two accretion events that led to maser variation in the outer arc and the inner arc of the western lobe would have occurred at an interval of about 3500 yr. If we use a higher shock velocity of 30 km s⁻¹, then the accretion events would have occurred at an interval of 2300 yr. In their numerical simulation of accretion-driven bursts in high mass

star formation, Meyer et al. (2017) found such accretion bursts to occur at intervals of 3000 yr, consistent with the calculation for DR21(OH) above. This means that if the shock that caused the increase in intensity of maser 30 reached the inner arc of the western lobe sometime after 2001, the shock that caused the increase in intensity of maser 4 in the outer arc would have reached it about 2300-3500 yr earlier (depending on how fast the shock was traveling). The modest increase in maser 4 after 2001 may be a lingering effect of this earlier shock, or it could be a result of the alternative scenarios discussed below.

Additional scenarios that can also cause variability in masers arise from changes in the path length over which the maser signal is amplified. One possibility is to assume that the maser region has an ellipsoidal shape and spins as a solid body with constant angular momentum so that there is velocity coherence along the line of sight, like Andreev et al. (2017) did to model the variation of formaldehyde (H_2CO) masers. As the maser region rotates (slowly), the amplification path changes and causes variations in the intensity of the maser. Another possibility is to assume a foreground cloud moving in front of a maser cloud, as Boboltz et al. (1998) did to model variation in H_2O masers in the high mass star forming region W49. This will also cause changes in the maser intensity. Both of these, a rotating maser cloud and a foreground cloud moving in front of a maser cloud, are initiated by turbulence, which can be caused by the very same shocks that are responsible for pumping Class I CH_3OH masers in outflows.

Turbulence is a random phenomenon, so we would expect roughly equal numbers of masers to increase and decrease in intensity in both the inner and outer arcs of the western lobe. For reasons described in the previous paragraphs, it is more likely that episodic accretion is causing the major differences in variation between the inner and outer arcs in the western lobe, although both processes could be active. Exceptions like maser 24 which decreased in intensity after 2001 (Section 4.2.2), and changes in maser intensities in the inner arc of the eastern lobe, could be caused by the changes in path length described above.

CHAPTER 5

Conclusions and Future Work

Using three different epochs spanning a 15-yr time period (2001, 2012, and 2017), I looked at the variability of 44 GHz Class I CH₃OH masers in DR21(OH). This, to my knowledge, is the first dedicated study of the variability of Class I CH₃OH masers in high mass star forming regions. Knowing the variability of such masers allows us to better understand the maser phenomenon, and such an understanding makes these masers a more effective probe of the high mass star formation process. Much remains to be learned about the process of high mass star formation, because high mass stars are rarer and located farther away from us. Masers are bright and compact sources and serve as excellent probes of high mass star forming regions at high angular resolution.

My analysis of data observed in 2017 with the VLA showed that the Class I CH₃OH masers in DR21(OH) are arranged in a western lobe and an eastern lobe, with two arcs in each lobe. This is consistent with previous observations. It is also consistent with the presence of Class I CH₃OH masers in outflows, where shocks provide the collisional pumping for such masers. I found a total of 57 masers in this region, with center velocities ranging between -8.65 km s^{-1} to $+2.56 \text{ km s}^{-1}$. These 57 masers include all the 24 redshifted masers observed in 2012 (Momjian & Sarma, 2017), and 48 of the 49 masers observed in 2001 (Araya et al., 2009). With a few exceptions, most of the masers in both the inner and the outer arcs in the western lobe increased in intensity from 2001 to 2012, then decreased from 2012 to 2017, or stayed constant. Most masers in the outer arc of the eastern lobe also increased in intensity. For the four masers in the inner arc of the eastern lobe for which data are available to compare, two out of four masers increased in intensity, whereas the other two decreased.

In particular, there is indication of significant variation in intensity for the two strongest masers in DR21(OH). From 2001 to 2012, maser 4 in the outer arc of the western lobe increased in intensity by a factor of 1.6, whereas maser 30 in the inner arc increased by 7.7 times. As a result, maser 4 became the second brightest maser in DR21(OH); it had been the brightest maser in 2001. Also as a result, maser 30 rose to become the brightest; it had been the second brightest maser in 2001. This, along with changes in intensity in several other masers, leads me to conclude with certainty that 44 GHz Class I CH₃OH masers do exhibit variability on long timescales of 5-10 yr.

At this stage there is insufficient observational evidence to come to any conclusions regarding the cause of the variability of these masers, other than that they exhibit variability on long timescales. I have presented two plausible scenarios that could cause such variability. One is that of episodic accretion, which is now known to occur in high mass stars while they are forming. Each such accretion burst is accompanied by an ejection event, which then creates the bowshocks in outflows such as those observed in DR21(OH). If the variability of the Class I CH₃OH masers in the inner and outer arcs of the western lobe of DR21(OH) has been caused by such an event, typical shock velocities would constrain these accretion events to be spread apart by about 3500 yr, which is consistent with the results of numerical simulations in the literature. There is certainly more activity going on in the inner arc of the western lobe compared to the outer arc to support this picture of a more recent shock to the inner arc that is causing these changes. Examples of such activity include larger increases in intensity and more new masers in the inner arc. Alternatively, changes in maser intensities could be a result of turbulence in the shocked regions. Such turbulence could cause ellipsoidal maser regions to rotate, or a foreground cloud to come in front of a maser region. Both of these would cause a change in the amplification path length and lead to variations in maser intensity.

Future work should focus on two fronts. The first would consist of establishing the variability of Class I CH₃OH masers in a larger number of regions. The second

front would entail looking for the causes of such variability. Extending to a larger number of regions would demonstrate how prevalent is the phenomenon of variability in Class I CH_3OH masers over the longer term. Looking for the causes of such variability would involve looking at other maser lines to see if they varied on similar timescales, and if the accretion event was recorded in some other tracer of thermal emission.

REFERENCES

- Andreev, N., Araya, E. D., Hoffman, I. M., et al. 2017, *ApJS*, 232, 29.
- Araya, E. D., Kurtz, S., Hofner, P., et al. 2009, *ApJ*, 698, 1321.
- Bachiller, R., Gomez-Gonzalez, J., Barcia, A., et al. 1990, *A&A*, 240, 116.
- Batrla, W., Matthews, H. E., Menten, K. M., et al. 1987, *Nature*, 326, 49.
- Boboltz, D. A., Simonetti, J. H., Dennison, B., et al. 1998, *ApJ*, 509, 256.
- Breen, S. L., Sobolev, A. M., Kaczmarek, J. F., et al. 2019, *ApJL*, 876, L25.
- Brogan, C. L., Hunter, T. R., Towner, A. P. M., et al. 2019, *ApJL*, 881, L39.
- Caratti o Garatti, A., Stecklum, B., Linz, H., et al. 2015, *A&A*, 573, A82.
- Caratti o Garatti, A., Stecklum, B., Garcia Lopez, R., et al. 2017, *Nature Physics*, 13, 276.
- Chandler, C. J., Moore, T. J. T., Mountain, C. M., et al. 1993, *MNRAS*, 261, 694.
- Comerón, F., Djupvik, A. A., Schneider, N., et al. 2020, *A&A*, 644, A62.
- Elitzur, M. 1992, *Astrophysics and Space Science Library*, Dordrecht: Kluwer, —c1992.
- Gordon, J. P., Zeiger, H. J., & Townes, C. H. 1955, *Physical Review*, 99, 1264.
- Gray, M. 2012, *Maser Sources in Astrophysics*: Cambridge University Press, 2012.
- Green, J. A., Breen, S. L., Fuller, G. A., et al. 2017, *MNRAS*, 469, 1383.
- Hunter, T. R., Brogan, C. L., MacLeod, G. C., et al. 2018, *ApJ*, 854, 170.
- Jones, B. M., Fuller, G. A., Breen, S. L., et al. 2020, *MNRAS*, 493, 2015.

- Kogan, L. & Slysh, V. 1998, *ApJ*, 497, 800.
- Kurtz, S., Hofner, P., & Alvarez, C. V. 2004, *ApJS*, 155, 149.
- Leurini, S., Menten, K. M., & Walmsley, C. M. 2016, *A&A*, 592, A31.
- Litovchenko, I. D., Alakoz, A. V., Val'Tts, I. E., et al. 2011, *Astronomy Reports*, 55, 1086.
- McCarthy, T. P., Ellingsen, S. P., Voronkov, M. A., et al. 2018, *MNRAS*, 477, 507.
- Menten, K. M. 1991, *Atoms, Ions and Molecules: New Results in Spectral Line Astrophysics*, 16, 119.
- Meyer, D. M.-A., Vorobyov, E. I., Kuiper, R., et al. 2017, *MNRAS*, 464, L90.
- Momjian, E. & Sarma, A. P. 2017, *ApJ*, 834, 168.
- Motte, F., Bontemps, S., Schilke, P., et al. 2007, *A&A*, 476, 1243.
- Plambeck, R. L. & Menten, K. M. 1990, *ApJ*, 364, 555.
- Pratap, P., Shute, P. A., Keane, T. C., et al. 2008, *AJ*, 135, 1718.
- Reid, M. J. & Moran, J. M. 1981, *ARAA*, 19, 231.
- Rodríguez-Garza, C. B., Kurtz, S. E., Gómez-Ruiz, A. I., et al. 2017, *ApJS*, 233, 4.
- Rygl, K. L. J., Brunthaler, A., Sanna, A., et al. 2012, *A&A*, 539, A79.
- Schneider, N., Bontemps, S., Motte, F., et al. 2016, *A&A*, 591, A40.
- Sobolev, A. M., Cragg, D. M., & Godfrey, P. D. 1997, *A&A*, 324, 211.
- Weaver, Harold, Williams, David R. W., Dieter, N. H., & Lum, W. T. 1965, *Nature*, 208, 29.
- Zapata, L. A., Loinard, L., Su, Y.-N., et al. 2012, *ApJ*, 744, 86.